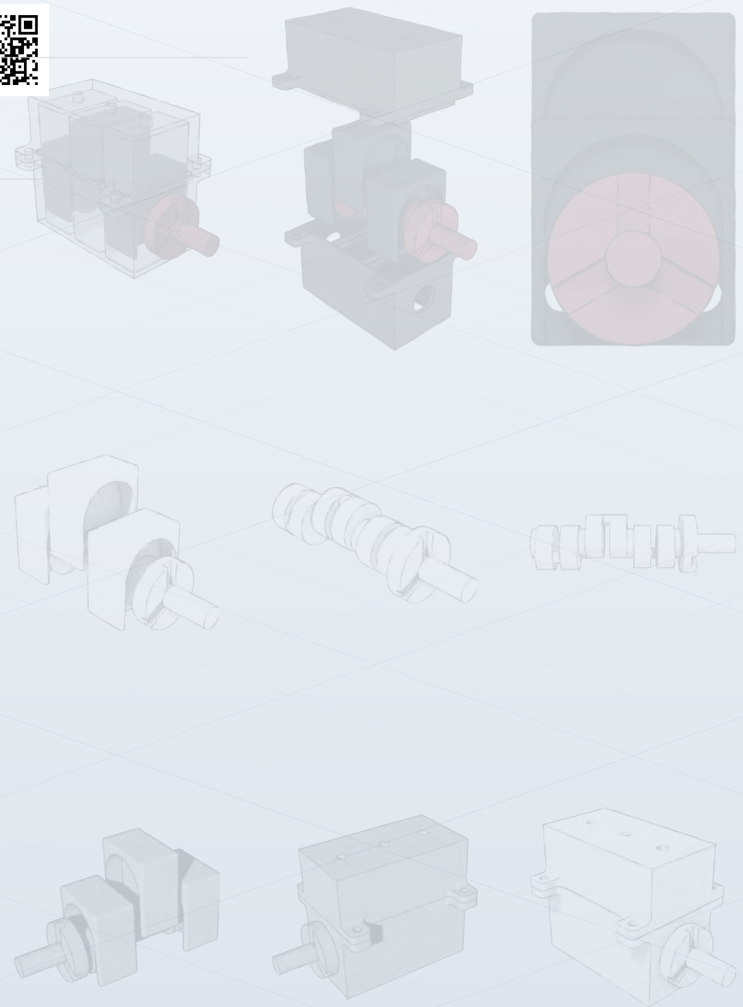

SRL.
UNIVERSITY OF TWENTE.

9 789036 565530

MAGNETIC RESONANCE COMPATIBLE PNEUMATIC ACTUATORS FOR SURGICAL ROBOTICS - FOAD S. FARIMANI

UT.

MAGNETIC RESONANCE COMPATIBLE PNEUMATIC ACTUATORS FOR SURGICAL ROBOTICS

FOAD S. FARIMANI

INVITATION

I cordially invite you
to attend the public defense
of my doctoral dissertation titled

Magnetic Resonance Compatible Pneumatic Actuators for Surgical Robotics

Monday, 2 June 2025
10:45

Prof. dr. G. Berkhoff-Zaal
Waaier building
University of Twente
Enschede, The Netherlands

MRI-Compatible · Additive Manufacturing
Pneumatic Actuation · Surgical Robotics
Friction Modeling · 3D Printing

f.s.farimani@utwente.nl

Paranymphs:
Mohammad Mozaffari Foumashi
Mehrdad Mohammadifakhr

Magnetic Resonance Compatible Pneumatic Actuators for Surgical Robotics

Foad Sojoodi Farimani

Monday 2nd June, 2025

MAGNETIC RESONANCE COMPATIBLE PNEUMATIC ACTUATORS FOR SURGICAL ROBOTICS

FOAD SOJOODI FARIMANI

MAGNETIC RESONANCE COMPATIBLE PNEUMATIC ACTUATORS FOR SURGICAL ROBOTICS

DISSERTATION

to obtain
the degree of doctor at the University of Twente,
on the authority of the rector magnificus,
prof. dr. ir. A. Veldkamp,
on account of the decision of the Doctorate Board,
to be publicly defended
on Monday the 2nd of June 2025 at 10.45 hours

by

Foad Sojoodi Farimani

born on the 21st of September, 1983
in Fariman, Iran

THIS DISSERTATION HAS BEEN APPROVED BY:

PROMOTOR PROF.DR. S. MISRA

Cover design: Foad S. Farimani
Printed by: Ipskamp Printing, Enschede
Lay-out: Foad S. Farimani
ISBN (print): 978-90-365-6553-0
ISBN (digital): 978-90-365-6554-7
URL: https://doi.org/10.3990/1.9789036565547

GRADUATION COMMITTEE:

Chair / secretary:

Prof. Dr. Ir. H.F.J.M. Koopman	University of Twente

Supervisor:

Prof. Dr. S. Misra	University of Twente, University of Groningen and University Medical Center Groningen

Committee Members:

Prof. Dr. J.J. van den Dobbelsteen	Delft University of Technology
Prof. Dr. I. Gibson	University of Twente
Prof. Dr. ir. M.B. de Rooij	University of Twente
Dr. A. Sadeghi	University of Twente
Dr. C. Moers	University Medical Center Groningen

To my precious family ...
My wife Fariba Ghaseny and my daughter Liana...

Summary

Magnetic Resonance Imaging (MRI)-guided surgical robotics offers unique advantages for minimally invasive interventions through superior soft tissue visualization without radiation. However, conventional electromagnetic actuators are incompatible with MRI scanners' strong magnetic fields. This dissertation develops novel Magnetic Resonance (MR)-compatible pneumatic actuators for surgical applications.

This research explores design, manufacturing, control, and tribological aspects of Pneumatic Stepper Motors (PSMs) for MRI-guided surgery, with special focus on frictional properties of Fused Deposition Modeling® (FDM)-printed surfaces. Understanding surface-friction relationships enables refined actuator design and control strategies, addressing inherent pneumatic nonlinearities.

Key contributions include:

- **Parametrically Optimized Design:** A methodology for customizable MR-compatible PSMs, adaptable to specific surgical requirements.
- **Hybrid Manufacturing:** Implementation of FDM and hybrid techniques for cost-effective fabrication with complex geometries and diverse materials.
- **Tribological Characterization:** Analysis of friction behavior in FDM-printed surfaces under various conditions for actuator optimization.
- **Advanced Control:** Development of pneumatic models and model-based control strategies for precise positioning in MRI environments.

The developed actuators demonstrated enhanced performance in prototypes, addressing key limitations in MR-compatible robotics. By enabling precise motion control within MRI constraints, this research advances surgical interventions and Minimally Invasive Surgery (MIS), with potential applications in other fields requiring precision in MRI environments.

Samenvatting

MRI-geleide chirurgische robotica biedt unieke voordelen voor minimaal invasieve ingrepen door superieure weefselvisualisatie zonder straling. Conventionele elektromagnetische actuatoren zijn echter onverenigbaar met MRI-scanners. Dit proefschrift ontwikkelt nieuwe MR-compatibele pneumatische actuatoren voor chirurgische toepassingen.

Dit onderzoek richt zich op ontwerp, productie, besturing en tribologie van PSM's voor MRI-geleide chirurgie, met nadruk op wrijvingseigenschappen van FDM-geprinte oppervlakken. Begrip van oppervlakte-wrijving relaties verfijnt actuatorontwerp en besturingsstrategieën, en adresseert pneumatische niet-lineariteiten.

Belangrijke bijdragen zijn:

- **Parametrisch Ontwerp:** Een methodologie voor aanpasbare MR-compatibele PSM's, afstembaar op chirurgische vereisten.
- **Hybride Fabricage:** Implementatie van FDM en hybride technieken voor kosteneffectieve productie met complexe geometrieën.
- **Tribologische Analyse:** Onderzoek naar wrijvingsgedrag in FDM-geprinte oppervlakken voor actuatoroptimalisatie.
- **Geavanceerde Besturing:** Ontwikkeling van pneumatische modellen en modelgebaseerde strategieën voor nauwkeurige positionering in MRI-omgevingen.

De ontwikkelde actuatoren toonden verbeterde prestaties in prototypes, en adresseren sleutelbeperkingen in MR-compatibele robotica. Door nauwkeurige bewegingsregeling binnen MRI-beperkingen mogelijk te maken, bevordert dit onderzoek chirurgische ingrepen en MIS, met potentiële toepassingen in andere vakgebieden die precisie in MRI-omgevingen vereisen.

Contents

II Principal Studies

III Concluding Remarks

List of Acronyms

ABS	Acrylonitrile Butadiene Styrene
AM	Additive Manufacturing
API	Application Programming Interface
AUT	AmirKabir University of Technology (formerly Tehran Polytechnic)
CA	Coulomb-Amontons
CAD	Computer Aided Design
CNC	Computer Numerical Control
CoF	Coefficient of Friction
COTS	Commercially available Off-The-Shelf
CT	Computed Tomography
DA	Direct-Acting
DOF	Degree of Freedom
DTI	Diffusion Tensor Imaging

EM	Electromagnetic
EPCU	Electro-Pneumatic Control Unit
FA	Flip Angle
FDM	Fused Deposition Modeling®
FLOSS	Free, Libre, and Open Source Software
fMRI	functional MRI
FOV	Field of View
GUI	Graphical User Interface
LPR	Light Puncture Robot
MIS	Minimally Invasive Surgery
MR	Magnetic Resonance
MRI	Magnetic Resonance Imaging
MST	Medisch Spectrum Twente
NSA	Number of Signal Averages
PanoSurg	**Pano**ramatic user interface for navigation and documentation of endoscopic guided **Surg**eries
PET	PolyEthylene Terephthalate
PiHC	Pioneers in Health-Care
PLA	PolyLactic Acid
PneuARMM	**Pneu**matically **A**ctuated **R**obot for **M**inimally invasive **M**RI-guided interventions
PSM	Pneumatic Stepper Motor
RaM	Robotics and Mechatronics
SLA	Stereolithography
SLS	Selective Laser Sintering
SM	Subtractive Manufacturing
SNR	Signal-to-Noise Ratio
SRL	Surgical Robotics Laboratory

SUT	Sharif University of Technology (formerly Aryamehr)
TB	Tabor-Bowden
TE	Echo Time
TR	Repetition Time
TU/e	Technical University of Eindhoven
USB	Universal Serial Bus
UT	University of Twente
ZGT	Ziekenhuis Groep Twente

I Prologue

1. Introduction

1.1 Background and motivation

Modern medicine has witnessed a remarkable transformation with the integration of robotics and mechatronics, leading to advancements in surgical precision, dexterity, and visualization that enhance human capabilities [1]. This has been particularly impactful in Minimally Invasive Surgery (MIS), where surgeons operate through smaller incisions, leading to less trauma, faster patient recovery, and improved outcomes compared to open surgery [2]. The da Vinci Surgical System® (figure 1.1) and similar robotic platforms have significantly impacted the adoption and advancement of minimally invasive surgery. They enable precise interventions within confined and hard-to-reach anatomical spaces, expanding the possibilities of MIS [3].

Among the various imaging modalities used to guide surgical interventions, Magnetic Resonance Imaging (MRI) stands out for its exceptional soft tissue contrast and the lack of ionizing radiation [5]. This makes MRI a valuable tool for visualizing critical anatomical structures and guiding surgical procedures with high precision. While MRI provides

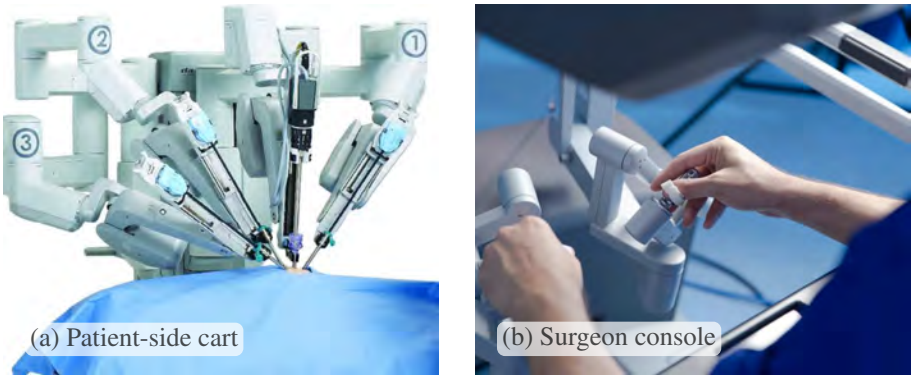

Figure 1.1: The da Vinci Surgical System® for minimally invasive surgery: (a) The patient-side cart with four robotic arms, enabling enhanced dexterity and access within confined surgical spaces. (b) The surgeon console featuring master controls that translate hand movements into precise motions of the robotic instruments. (Images are used under CC BY 3.0 license [4]).

valuable intraoperative imaging feedback without using ionizing radiation, its magnetic field poses a significant challenge for conventional robotic systems that rely on Electromagnetic (EM) actuators [6, 7]. This EM interference disrupts imaging quality and robot functionality, hindering the widespread adoption of MRI-guided robotic surgery.

To address this challenge, the present doctoral research investigates pneumatic actuation as a promising alternative to EM actuators for MRI-guided robotic surgery. Pneumatic systems, driven by compressed air, offer inherent compatibility with MRI environments, eliminating the risk of EM interference. Furthermore, the abundance of pressurized and sterilized air in all hospitals makes pneumatic actuation particularly suitable for delicate surgical procedures [8].

While various types of pneumatic actuators exist, such as vane motors and piston cylinders, they often lack the precision and controllability required for surgical applications [9, 10]. On the other hand, Pneumatic Stepper Motors (PSMs) present a promising approach (table 1.1[1]) by

[1]This table represents the state of the art up to 2020, reflecting the timeframe of the doctoral research presented in this dissertation. While efforts were made to include recent developments, the rapidly evolving nature of the field may have led to unintentional omissions. The author acknowledges the ongoing contributions of researchers in this area.

combining air-powered actuation with mechanical discretization, enabling precise open-loop position regulation [11]. Recent advancements in integrating feedback mechanisms into PSMs further enhance their accuracy and reliability, paving the way for closed-loop control systems that meet the stringent demands of surgical robotics [12, 13].

Despite the potential of PSMs, previous attempts at creating Magnetic Resonance (MR)-compatible versions have faced limitations in terms of cost-effectiveness, performance, and manufacturability. This research addresses these limitations by leveraging the capabilities of Additive Manufacturing (AM) to create customized and optimized PSMs specifically tailored for MRI-guided surgical applications.

Furthermore, this research investigated the tribology of 3D-printed surfaces to understand how material properties and manufacturing parameters influence friction [14]. This knowledge is crucial for optimizing the design and performance of 3D-printed actuators and mechanisms used in high-precision applications like surgical robotics [15].

By harnessing the potential of AM and advanced control strategies, this dissertation strives to unlock the potential of MR-compatible pneumatic actuation, contributing to safer, more affordable, and more accessible MRI-guided robotic surgery [16]. This, in turn, promises to improve surgical precision, reduce patient trauma, and ultimately enhance patient care and outcomes [2].

1.2 Historical Overview

The integration of robotics with medical imaging, especially MRI, has significantly advanced the field of MIS [17, 18]. Combining robotics with MRI allows practitioners to perform more accurate and less invasive interventions with real-time image guidance [17]. One primary advantage of MRI-guided robots is their ability to track anatomical structures, instruments, and therapy delivery during surgery. This closed-loop system allows for real-time adjustments based on intraoperative feedback instead of relying solely on static preoperative imaging [17]. This real-time guidance during interventions enhances precision by enabling surgeons to monitor instrument navigation and tissue deflection during procedures [18]. However, the benefits of MRI-guided robotics are accompanied by significant challenges. MRI scanners utilize strong

magnetic fields, creating an inherently incompatible environment with conventional robotic systems [19, 20]. The strong magnetic fields preclude using standard ferromagnetic materials in actuators and other robot components [20, 21], and EM actuators and conductive elements used in traditional robots are incompatible with MRI scanners due to EM interference [20, 21]. These limitations have spurred the development of specialized robotic systems and actuation methods specifically designed for MR compatibility [17, 19, 20, 22]. These systems often incorporate alternative materials and actuators to function effectively within the MRI environment [17, 23].

Pioneering efforts in the late 1990s and early 2000s focused on demonstrating the feasibility of MR-compatible robotics for various surgical applications. One notable example is the MrBot system, developed at the Johns Hopkins University (USA) for prostate brachytherapy [26]. MrBot employs three orthogonal pairs of pistons arranged in an oblique cylindrical configuration for precise needle guidance and includes integrated tracking coils in its end-effector that enable real-time position monitoring with six degrees of freedom at 20 Hz (figure 1.2). Remotely controlled using tailor-made PSM, PneuStep, MrBot prioritizes simplicity, cost-effectiveness, robustness, and safety. Its development progressed rapidly from concept to clinical trials, treating many patients undergoing prostate biopsy and seed placement procedures by 2008. Another pioneering effort was developed by Masamune *et al.* (1995) [25], a robot for neurosurgical applications. The 6-Degree of Freedom (DOF) robot, designed for MR-guided stereotactic needle biopsies, featured a frame made primarily of MRI-inert PolyEthylene Terephthalate (PET) and was actuated by ultrasonic motors. While demonstrating feasibility, this research highlighted challenges related to material stiffness and image degradation caused by the actuators [8, 17–20, 27]. While these early MRI-guided systems faced limitations in dexterity, workspace, and real-time position updates due to patient access constraints and long image acquisition times [28], they paved the way for advancements in hardware, pulse sequences, and user interfaces, leading to more open systems with rapid imaging capabilities and propelling the field towards further progress.

One prominent approach in MR-compatible robotics favors pneumatic actuators over hydraulic systems due to their inherent safety, high power-to-weight ratio, cleanliness, and speed [19]. While well-suited for ap-

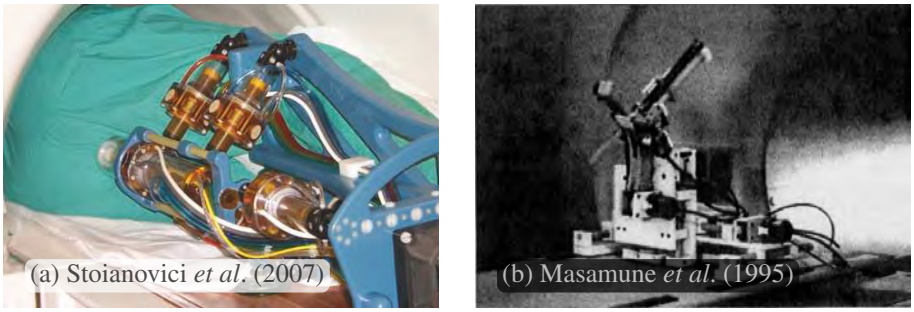

Figure 1.2: Pioneering Magnetic Resonance (MR)-compatible Robotic Systems: (a) The MrBot system, developed by Stoianovici *et al*. (2007) [24], designed for transperineal prostate interventions in the Magnetic Resonance Imaging (MRI) environment. (b) The MR-compatible robot for neurosurgical applications, developed by Masamune *et al*. (1995) [25], showcasing early innovations in MRI-guided stereotactic procedures. These systems represent significant early efforts to integrate robotic assistance with MRI guidance for surgical interventions.

plications requiring relatively low force, continuous servo pneumatic systems offer limited controllability due to air compressibility. They often utilize readily available pressurized air supplies in MRI suites and can incorporate MR-compatible pneumatic cylinders [18]. However, traditional pneumatic cylinders, designed for movement between two limit positions, face challenges in achieving accurate and precise position control at intermediate locations due to air compressibility, bandwidth limitations, and motion delays. The INNOMOTION system, developed by Innomedic (Herxheim, Germany), exemplifies the use of pneumatic cylinder drives in an MR-compatible robotic assistance system, featuring a 6-DOF MR-safe robot arm maneuverable within a closed-bore MRI scanner [29].

PSMs are a promising actuation method for MR-compatible robotic systems, offering precise motion control without EM interference. PSM designs for these applications utilize various principles, including nutation motors, wobble motors (i.e., harmonic drives), two-stroke engines, and incorporate Direct-Acting (DA) gears for enhanced simplicity and robustness [5, 12, 37, 38, 40, 41]. These motors vary significantly in size and torque output, reflecting a balance between performance require-

Table 1.1: Evolution of Pneumatic and Hydraulic Actuators in Medical Robotics (1998-2020)

This table provides a comparative analysis of key features across various studies, highlighting the progression in incorporating Electromagnetic (EM) stealth, volumetric, stepping capabilities, and Additive Manufacturing (AM) techniques. A green checkmark (✓) indicates the presence of a feature, a red cross (✗) indicates its absence, and a yellow tilde (∼) denotes partial or developing implementation. Early research by Suzumori *et al*. (1998) and others (figure 1.3) focused on converting continuous fluidic motion into discrete rotational steps, later incorporating Magnetic Resonance (MR) compatibility, as seen in the work of Suminski *et al*. (2002) and Taillant *et al*. (2004) [31–36]. Further advancements integrated volumetric and stepping capabilities, as demonstrated by the pneumatic step motors of Stoianovici *et al*. (2007) [24] and the MR-safe pneumatic rotation stepping actuator of Sajima *et al*. (2010) [37, 38]. The emergence of AM, pioneered by Slightam *et al*. (2012) [39] using selective laser sintering, opened new avenues for creating intricate actuator designs. These efforts culminated in the development of fully 3D-printed, assembly-printed, and MR-compatible pneumatic stepper actuators, such as PneuAct, introduced in 2018, addressing affordability, disposability, high resolution, and safe backdrivability for Magnetic Resonance Imaging (MRI)-guided surgical applications [16]. Similarly, Boland *et al*. (2019) [11] presented a four-cylinder piston Pneumatic Stepper Motor (PSM) fabricated using stereolithography, further demonstrating the feasibility of 3D printing for creating MR-compatible actuators. These advancements highlight the continuous pursuit of improving performance, reducing size, and enhancing safety and reliability in PSM design for MR-compatible robotics.

Year	1998	2002	2004	2007	2007	2007	2008	2010	2012	2014	2015	2016		2017	2018	2019	2020
First Author	Suzumori	Suminski	Taillant	Suminski	Elhawary	Stoianovici	Tse	Sajima	Slightam	Chen	Secoli	Wineland	Comber	Wei Chen	Farimani	Boland	Farimani
Stealth	✗	✓	✓	✓	✓	✓	✓	✓	✓	✓	✓	∼	✓	✓ ✓	✓	✓	✓
Volumetric	✓	✓	✓	✓	✗	✓	✗	✓	✓	✓	✓	✓	✓	✗ ✗	✓	✓	✓
Stepper	✓	✗	✓	✗	✗	✓	✗	✓	✗	✓	✓	✓	✓	∼ ✗	✓	✓	✓
AM	✗	✗	✗	✗	✗	✗	✗	✗	✓	✗	✗	✗	✗	✓ ✗	✓	✓	✓
Non-assembly	✗	✗	✗	✗	✗	✗	✗	✗	✗	✗	✗	✗	✗	✓ ✗	✓	✗	✗

First EM stealth ← First AM ← First non-assembly printing ←

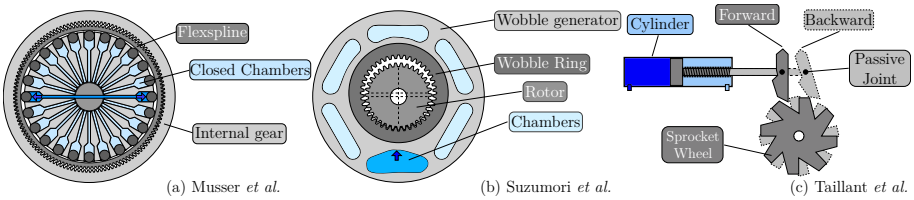

Figure 1.3: Conceptual schematics of early Pneumatic Stepper Motor (PSM) designs: (a) The design of Musser (1963) [30] utilizes a series of closed radial chambers that deform a flexspline upon radial expansion, engaging with an internal gear to generate rotational motion. (b) The concept of Suzumori *et al*. (1998) [31] employs six concentrically arranged chambers and an internal gear set to convert reciprocating motion into rotation. (c) The mechanism of Taillant *et al*. (2004) [32] features a solid articulated head connected to a piston, which pushes a sprocket wheel to create rotational stepping motion.

ments, miniaturization, and precision, with design choices dictated by the specific robotic application. A notable example is the PneuStep motor, based on a wobble motor design, offering high resolution and torque but with increased complexity and potential for MRI image artifacts [24]. Miniature actuators prioritizing compactness, such as one with a 10 mm diameter and only seven moving parts, sacrifice bidirectional movement for size reduction. Research and development efforts continue to enhance PSMs for MR-compatible robotics, focusing on improving performance, reducing size, and enhancing safety and reliability. These advancements prioritize MR-conditional materials like plastics, non-ferromagnetic metals, and specialized components such as fiber optic encoders to ensure compatibility with the MRI environment.

Piezoelectric motors have also been explored for MR-compatible robotic systems, offering high precision and fast response times [18, 42]. Researchers have investigated their potential in delicate surgical tasks, particularly in neurosurgery [25] and breast interventions [43, 44]. However, challenges associated with piezoelectric motors, such as potential image distortion due to their electrical nature and the need for effective insulation [45], have led to exploring alternative actuation methods.

Hydraulic actuation, known for its high-force capabilities, has also been considered for MR-compatible robotics [42]. By placing the hydraulic power source outside the MRI room and using non-magnetic and non-

conductive materials for motion transmission, researchers have aimed to address EM interference concerns [18, 46]. However, the complexity of hydraulic systems and the risk of fluid leakage pose ongoing challenges.

The development of MR-compatible robotic systems has also focused on improving sensing technologies, control algorithms, and system integration. Researchers have explored using optical encoders [24, 47, 48], fiber optic sensors [49, 50], and other non-magnetic sensing modalities [42, 51] for position feedback and control [18]. Additionally, advanced control strategies, such as model-based [52] and adaptive control [53], have been implemented to address the nonlinearities and complexities associated with alternative actuation methods, enhancing the precision and reliability of these systems.

Despite the significant progress in MR-compatible robotics, several challenges remain. Many existing systems are limited in their dexterity, workspace, and force capabilities compared to traditional robotic systems designed for non-MRI environments [23]. Achieving high precision and reliability in control remains an ongoing research focus, especially for complex interventions [6]. Developing robust, miniaturized, and cost-effective MR-compatible sensing technologies is crucial for further advancing the field and facilitating the wider adoption of these innovative surgical platforms [45, 47].

1.3 Objectives and Research Questions

The overarching goal of this dissertation is to advance the field of MR-compatible surgical robotics by developing and optimizing novel pneumatic actuators specifically tailored for surgical applications within the constraints of MRI environments. To achieve this, the research focuses on four key areas, each represented by a central research question and its corresponding objectives:

In our parametric design approach, we focused primarily on critical dimensions such as clearances between components. These clearances—whether between the crankshaft and pistons or between the pistons and cylinder walls—were particularly important for assembly-printed components. We needed to ensure clearances were large enough to prevent fusion of separately designed parts during printing, while keeping them tight enough for mechanical precision and pneumatic efficiency. Too large

a clearance between the crankshaft and pistons would introduce uncertainty and reduce system lifespan, while excessive clearance between pistons and cylinders would compromise the airtightness of the pressurized chamber. The crankshaft radius was also parametrically linked to the dimensions of the pistons themselves. While the entire design was parametric regardless of the Computer Aided Design (CAD) software used (FreeCAD with Python Application Programming Interface (API), SolidWorks, or Fusion 360), our primary focus was on optimizing these specific clearance parameters rather than conducting a comprehensive parametric exploration of all possible variables.

1: Conceptual Design and Parametric Modeling

Research Question: Can we design a pneumatic stepper actuator using rapid manufacturing that offers customizable performance, affordability, disposability, backdrivability, and deterministic behavior for surgical robotics?

Objectives:

1 Design a novel pneumatic stepper actuator optimized for accessible manufacturing methods, including 3D printing, desktop Computer Numerical Control (CNC) machining, and laser cutting.
2 Implement a parametric design methodology enabling customization of dimensions and performance characteristics based on application requirements.
3 Explore innovative mechanisms for achieving reliable stepping motion and backdrivability.

2: Additive Manufacturing and Hybrid Fabrication

Research Question: How can AM and hybrid fabrication techniques improve the performance, cost-effectiveness, and customizability of PSMs for surgical robots?

Objectives:

4 Explore different AM technologies for fabricating PSM components.
5 Investigate hybrid manufacturing techniques to enhance surface quality, dimensional accuracy, and overall performance.
6 Develop a framework for optimizing AM and hybrid fabrication methods based on actuator requirements.

3: Tribology of AM Surfaces

Research Question: How do surface characteristics and operating conditions influence friction in 3D printed components, and how can this knowledge improve mechatronic systems?

Objectives:

7 Characterize tribological properties of 3D-printed surfaces under various conditions.
8 Analyze effects of AM process parameters on surface roughness and friction.
9 Evaluate and modify friction models to accurately predict behavior in additively manufactured surfaces.

4: Control of Pneumatic Actuators in MRI

Research Question: How can model-based control techniques effectively regulate PSM for surgical robots in MRI environments, enhancing precision and safety?

Objectives:

10 Develop models capturing the pneumatic system's dynamics and MRI interactions.
11 Design model-based control strategies for precise position control.
12 Evaluate control system performance through experiments and simulations.

Our hybrid manufacturing approach maintained AM (3D printing) as the core production method while incorporating post-processing and integration of Commercially available Off-The-Shelf (COTS) components. Specifically, we implemented CNC machining on critical 3D-printed surfaces—particularly the internal cylinder walls—to improve surface finish, reduce friction, and enhance pneumatic airtightness. We also explored surface treatment using environmentally controlled chambers with acetone to further improve the surface quality of components. Additionally, we integrated COTS parts for specific sub-systems, such as the gearing mechanism, rather than fully 3D printing them. This represents a departure from our initial goal of complete assembly printing, but this specific hybrid approach (Fused Deposition Modeling® (FDM) + CNC machining + selected COTS components) proved beneficial for creating practical and reliable actuators.

This dissertation systematically investigates these research questions,

contributing to the fields of MR-compatible pneumatic actuation and tribology of AM surfaces. The findings from this research will provide a foundation for developing new, highly adaptable mechatronic systems for surgical robotics, ultimately leading to improved precision, safety, and accessibility in minimally invasive interventions.

1.4 Contributions and Outline

This dissertation contributes to the field of MR-compatible surgical robotics by addressing the critical challenge of actuator design and control. The research advances the state-of-the-art in electromagnetically stealth mechatronics through the development of innovative pneumatic actuators, a comprehensive understanding of the tribological behavior of 3D-printed surfaces, and the implementation of advanced control strategies.

Key contributions include:

-
- **Parametrically Optimized Actuator Design:** This dissertation implements a parametric design approach for MR-compatible PSM, focusing on key dimensions such as clearances and piston geometry to enable customization of actuator specifications based on specific surgical requirements. [Chapters 2 and 4]
- **Additive and Hybrid Manufacturing for Actuator Fabrication:** This research demonstrates a specific hybrid approach combining FDM with post-CNC machining of critical surfaces to fabricate PSM components with improved surface finish, reduced friction, and enhanced pneumatic efficiency. [Chapters 2 and 4]
- **Tribological Characterization of 3D-Printed Surfaces:** This research comprehensively analyzes the friction and wear behavior of FDM-printed surfaces under various conditions to develop a refined friction model and inform the design and control of 3D-printed actuators. [Chapter 3]
- **Modeling and Control for Pneumatic Actuators:** This dissertation develops models and implements model-based control strategies for PSM to achieve precise and robust position control for surgical applications. [Chapter 4]

The parametric design approach utilized in this work focused primarily

on key dimensions such as clearances between components (particularly between the crankshaft and pistons, and between the pistons and cylinder walls), piston dimensions, and crankshaft radius. While the entire design was parametric, specific attention was given to these critical parameters to balance manufacturing constraints with performance requirements. This approach not only facilitated the research and development process by allowing performance optimization through dimensional adjustments, but also supported patient-centric design by enabling end users to adapt actuator specifications to different anatomies and surgical applications without requiring complete redesign.

The hybrid manufacturing approach implemented in this research maintained FDM as the core production method while incorporating post-processing and integration of COTS components. Specifically, CNC machining was applied to critical 3D-printed surfaces—particularly the internal cylinder walls—to improve surface finish, reduce friction, and enhance pneumatic airtightness. This specific hybrid approach addressed the limitations of purely FDM-printed surfaces by reducing the chaotic nature of friction and improving the deterministic behavior of the actuators. The resulting improvement in both performance and predictability was particularly important for surgical applications, while still maintaining the cost-effectiveness and design flexibility that are unique advantages of additive manufacturing.

The dissertation is structured as follows:

- **Part I Prologue:** establishes the foundation for the research by providing background information, motivation, research objectives, and a review of relevant literature.
  - **Chapter 1 Introduction:** introduces the challenge of actuator design in MRI-guided surgical robotics. Outlines the research objectives and questions. Highlights the potential contributions of this dissertation.
- **Part II Principal Studies:** showcases published research on developing and characterizing PneuAct PSM for MR-compatible surgical robotics.
  - **Chapter 2 Introducing PneuAct I:** presents the design and initial testing of PneuAct I, a customizable, affordable, and safe 3D-printed PSM. Demonstrates the feasibility of using additive manufacturing for MR-compatible actuators. High-

lights the potential for cost-effective and tailored solutions in surgical robotics.
  - **Chapter 3 Friction of FDM Surfaces:** investigates the frictional behavior of 3D-printed surfaces. Reveals limitations of conventional friction models and proposes modified models. Demonstrates that friction decreases at higher speeds, likely due to reduced dwell time and chaotic vibrations.
  - **Chapter 4 Introducing PneuAct-II:** details the development and evaluation of PneuAct II, a PSM utilizing hybrid manufacturing. Demonstrates improved performance and resolution for MR-compatible surgical robots. Showcases the benefits of combining additive and subtractive manufacturing for achieving higher actuator precision and efficiency.
- **Part III Concluding Remarks:** synthesizes the key findings and contributions of this dissertation.
  - **Chapter 5 Conclusions:** revisits the research questions and objectives. Offers insights into future research directions. Provides a comprehensive overview of advancements in the field of MR-compatible surgical robotics.

This dissertation integrates knowledge from various disciplines, including mechatronics, tribology, and AM, to advance the field of MR-compatible surgical robotics. The developed actuators, friction models, and control strategies offer significant potential for improving surgical precision, safety, and accessibility. Furthermore, the novel approaches presented in this work address critical challenges in the development of MR-compatible systems, particularly in terms of material selection, manufacturing processes, and system integration. These contributions not only enhance the current state of surgical robotics but also pave the way for future innovations in image-guided interventions, ultimately contributing to the advancement of patient care and clinical outcomes.

1.5 Research Framework and Scientific Outputs

The research presented in this dissertation was conducted within the stimulating and collaborative environment of the Surgical Robotics Laboratory (SRL) at the University of Twente (UT), The Netherlands. Under the mentorship of Professor Sarthak Misra, the SRL focuses on developing innovative robotic technologies for surgical applications, particularly

minimally invasive interventions and image-guided procedures. The laboratory is equipped with state-of-the-art facilities for designing, prototyping, and testing robotic systems, including 3D printers, CNC machines, and laser cutters. Additionally, the SRL promotes strong collaborations with clinical partners, such as the Medisch Spectrum Twente (MST) hospital, providing valuable insights into clinical needs and facilitating the translation of research findings into practical applications.

In addition generous financial support from the University of Twente, this doctoral research was supported by various funding sources and collaborative projects, including:

- A Pioneers in Health-Care (PiHC) voucher for the **Pneu**matically **A**ctuated **R**obot for **M**inimally invasive **M**RI-guided interventions (PneuARMM) project [54]: This collaborative effort between the UT, MST hospital, and PneuRobotics provided crucial funding and framework. It supported the development and evaluation of novel pneumatic actuator technologies and robotic systems central to this dissertation.
- PiHC voucher for the Enhanced Reality **Pano**ramatic user interface for navigation and documentation of endoscopic guided **Surg**eries (PanoSurg) project [55]: This initiative, including UT and Ziekenhuis Groep Twente (ZGT), focused on developing innovative user interfaces for robotic-assisted surgery. It aimed to address the challenge of limited visualization in endoscopic procedures, enhancing surgeon capabilities and patient outcomes.

The scientific output of this dissertation is disseminated through the following peer-reviewed publications:

- **Introducing PneuAct: Parametrically Designed MRI-Compatible Pneumatic Stepper Actuator**. F. Sojoodi Farimani and S. Misra. In proceedings of the IEEE International Conference on Robotics and Automation (ICRA), Brisbane, Australia, April 2018, pages 200–205.
- **PneuAct-II: Hybrid Manufactured Electromagnetically Stealth Pneumatic Stepper Actuator**. F. Sojoodi Farimani, M. Mojarradi, E. Hekman, and S. Misra. IEEE Robotics and Automation Letters (RA-L), volume 5, issue number 2, April 2020, pages 3588–3593.
- **Frictional Characteristics of Fusion Deposition Modeling (FDM)**

Manufactured Surfaces. F. Sojoodi Farimani, M. de Rooij, E. Hekman, and S. Misra. Rapid Prototyping Journal (RPJ), volume 26, issue number 6, May 2020, pages 1095–1102.

These publications showcase the key advancements in MR-compatible pneumatic actuators and their potential for application in surgical robotic systems.

References

[1] Alvey. "Robotics in Healthcare | HIMSS". *Online Journal of Nursing Informatics (OJNI)*. 2021.

[2] Goh *et al*. "Robotic surgery: an evolution in practice". *Journal of Surgical Protocols and Research Methodologies*. Vol. 2022, No. 1, snac003. 2022.

[3] Kao *et al*. "When Does Da Vanci Robotic Surgical Systems Come Into Play?" *Frontiers in Public Health*. Vol. 10, page 828542. 2022.

[4] Beasley. "Medical Robots: Current Systems and Research Directions". *Journal of Robotics*. Vol. 2012, page 401613. 2012.

[5] Elhawary *et al*. "A Review of Magnetic Resonance Imaging Compatible Manipulators in Surgery". *Proceedings of the Institution of Mechanical Engineers, Part H: Journal of Engineering in Medicine*. Vol. 220, No. 3, pages 413–424. 2006.

[6] Fisher *et al*. "Intraoperative magnetic resonance imaging–conditional robotic devices for therapy and diagnosis". *Proceedings of the Institution of Mechanical Engineers, Part H: Journal of Engineering in Medicine*. Vol. 228, No. 3, pages 303–318. 2014.

[7] Schenck. "The role of magnetic susceptibility in magnetic resonance imaging: MRI magnetic compatibility of the first and second kinds". *Medical Physics*. Vol. 23, No. 6, pages 815–850. 1996.

[8] Xiao *et al*. "MR-Conditional Actuations: A Review". *Annals of Biomedical Engineering*. Vol. 48, No. 12, pages 2707–2733. 2020.

[9] Carfagni *et al*. "A vane-motor automatic design procedure". *International Journal on Interactive Design and Manufacturing (IJIDeM)*. Vol. 7, No. 3, pages 147–157. 2013.

[10] Kulkarni *et al*. "Review of Robotic Needle Guide Systems for Percutaneous Intervention". *Annals of Biomedical Engineering*. Vol. 47, No. 12, pages 2489–2513. 2019.

[11] Boland *et al*. "High Speed Pneumatic Stepper Motor for MRI Applications". *Annals of Biomedical Engineering*. Vol. 47, No. 3, pages 826–835. 2019.

[12] Secoli *et al*. "A low-cost, high-field-strength magnetic resonance imaging–compatible actuator". *Proceedings of the Institution of Mechanical Engineers, Part H: Journal of Engineering in Medicine*. Vol. 229, No. 3, pages 215–224. 2015.

[13] Rossides. “Design and Implementation of a Modular, Customizable, Multi-Modality Compatible Actuator with Position Feedback”. Master’s thesis. Enschede, The Netherlands: University of Twente, Robotics and Mechatronics, Aug. 2016.

[14] Sojoodi Farimani *et al*. “PneuAct-II: Hybrid Manufactured Electromagnetically Stealth Pneumatic Stepper Actuator”. *IEEE Robotics and Automation Letters*. Vol. 5, No. 2, pages 3588–3593. 2020.

[15] Leacock *et al*. “Structural and Frictional Performance of Fused Deposition Modelled Acrylonitrile Butadiene Styrene (P430) with a view to use as Rapid Tooling Material in Sheet Metal Forming.” *Key Engineering Materials*. Vol. 639, pages 325–332. 2014.

[16] Sojoodi Farimani *et al*. “Introducing PneuAct: Parametrically-Designed MRI-Compatible Pneumatic Stepper Actuator”. In: *Proc. IEEE Int. Conf. on Robotics and Automation (ICRA)*. Pages 200–205. 2018.

[17] Su *et al*. “State of the Art and Future Opportunities in MRI-Guided Robot-Assisted Surgery and Interventions”. *Proceedings of the IEEE*. Vol. 110, No. 7, pages 968–992. 2022.

[18] Elhawary *et al*. “The case for MR-compatible robotics: a review of the state of the art”. *The International Journal of Medical Robotics and Computer Assisted Surgery*. Vol. 4, No. 2, pages 105–113. 2008.

[19] Tsekos *et al*. “Magnetic Resonance–Compatible Robotic and Mechatronics Systems for Image-Guided Interventions and Rehabilitation: A Review Study”. *Annual Review of Biomedical Engineering*. Vol. 9, pages 351–387. 2007.

[20] Taylor *et al*. “Medical robotics in computer-integrated surgery”. *IEEE Transactions on Robotics and Automation*. Vol. 19, No. 5, pages 765–781. 2003.

[21] Fütterer *et al*. “MRI of the prostate: potential role of robots”. *Imaging in Medicine*. Vol. 2, No. 5, page 583. 2010.

[22] Pondman *et al*. “MR-Guided Biopsy of the Prostate: An Overview of Techniques and a Systematic Review”. *European Urology*. Vol. 54, No. 3, pages 517–527. 2008.

[23] Gassert *et al*. “MRI-compatible robotics”. *IEEE Engineering in Medicine and Biology Magazine*. Vol. 27, No. 3, pages 12–14. 2008.

[24] Stoianovici *et al*. “A New Type of Motor: Pneumatic Step Motor”. *IEEE/ASME Transaction on Mechatronics*. Vol. 12, No. 1, pages 98–106. 2007.

[25] Masamune *et al*. "Development of an MRI-Compatible Needle Insertion Manipulator for Stereotactic Neurosurgery". *Image Guided Surgery*. Vol. 1, No. 4, pages 242–248. 1995.

[26] Kettenbach *et al*. "Ultrasound-, CT- and MR-Guided Robot-Assisted Interventions". In: *Image Processing in Radiology: Current Applications*. Edited by Neri *et al*. Berlin, Heidelberg: Springer Berlin Heidelberg, 2008, pages 393–409.

[27] Fischer *et al*. "MRI Compatibility of Robot Actuation Techniques – A Comparative Study". In: *Medical Image Computing and Computer-Assisted Intervention – MICCAI 2008*. Pages 509–517. 2008.

[28] Weiss *et al*. "MR-guided biopsy: A review of current techniques and applications". *Journal of Magnetic Resonance Imaging*. Vol. 27, No. 2, pages 311–325. 2008.

[29] Melzer *et al*. "MR-Guided Interventions and Surgery". In: *Springer Handbook of Medical Technology*. Edited by Kramme *et al*. Berlin, Heidelberg: Springer Berlin Heidelberg, 2011, pages 477–501.

[30] Musser. "Fluid wave generator for harmonic drive". U.S. Patent 3088333. May 7, 1963.

[31] Suzumori *et al*. "A direct-drive pneumatic stepping motor for robots: designs for pipe-inspection microrobots and for human-care robots". In: *Proc. IEEE Int. Conf. on Robotics and Automation (ICRA)*. Vol. 4, pages 3047–3052. 1998.

[32] Taillant *et al*. "CT and MR Compatible Light Puncture Robot: Architectural Design and First Experiments". In: *Medical Image Computing and Computer-Assisted Intervention – MICCAI 2004: 7th International Conference, Saint-Malo, France, September 26-29, 2004. Proceedings, Part II*. Edited by Barillot *et al*. Berlin, Heidelberg: Springer, 2004, pages 145–152.

[33] Suminski *et al*. "A pneumatically actuated manipulandum for neuromotor control research". In: *Proceedings of the Second Joint 24th Annual Conference and the Annual Fall Meeting of the Biomedical Engineering Society, Engineering in Medicine and Biology*. Vol. 3, pages 2347–2348. 2002.

[34] Suzumori *et al*. "Pneumatic direct-drive stepping motor for robots". In: *IEEE/RSJ International Conference on Intelligent Robots and Systems*. Vol. 2, pages 2031–2036. 2002.

[35] Suzumori *et al*. "Nutation motor new direct-drive stepping motor for robots". In: *IEEE Conference on Robotics and Automation, 2004. TExCRA Technical Exhibition Based.* Pages 21–22. 2004.

[36] Suminski *et al*. "Design and validation of a MR-compatible pneumatic manipulandum". *Journal of Neuroscience Methods*. Vol. 163, No. 2, pages 255–266. 2007.

[37] Sajima *et al*. "Two-DOF non-metal manipulator with pneumatic stepping actuators for needle puncturing inside open-type MRI". In: *World Automation Congress*. Pages 1–6. 2010.

[38] Sajima *et al*. "MR-safe pneumatic rotation stepping actuator". *Journal of Robotics and Mechatronics*. Vol. 24, No. 5, pages 820–827. 2012.

[39] Slightam *et al*. "Novel integrated fluid-power actuators for functional end-use components and systems via selective laser sintering nylon". In: *23rd Ann Int Solid Freeform Fabrication Symp*. Pages 197–211. 2012.

[40] Chen *et al*. "An MR-Conditional High-Torque Pneumatic Stepper Motor for MRI-Guided and Robot-Assisted Intervention". *Annals of Biomedical Engineering*. Vol. 42, No. 9, pages 1823–1833. 2014.

[41] Zhi. "Design and Prototyping of McRobot Version 3.1: Multi-modality Compatible Robot for Image Guided Minimally Invasive Intervention and Therapy". Master's thesis. Enschede, The Netherlands: University of Twente, Robotics and Mechatronics, Aug. 2015.

[42] Gassert *et al*. "Actuation methods for applications in MR environments". *Concepts in Magnetic Resonance Part B: Magnetic Resonance Engineering*. Vol. 29B, No. 4, pages 191–209. 2006.

[43] Louw *et al*. "Surgical robotics: a review and neurosurgical prototype development". *Neurosurgery*. Vol. 54, No. 3, pages 525–537. 2004.

[44] Larson *et al*. "Design of an MRI-Compatible Robotic Stereotactic Device for Minimally Invasive Interventions in the Breast†". *Journal of Biomechanical Engineering*. Vol. 126, No. 4, pages 458–465. 2004.

[45] Chinzei *et al*. "MR Compatibility of Mechatronic Devices: Design Criteria". In: *Medical Image Computing and Computer-Assisted Intervention – MICCAI'99*. Pages 1020–1030. 1999.

[46] Stoianovici. "Multi-imager compatible actuation principles in surgical robotics". *The International Journal of Medical Robotics and Computer Assisted Surgery*. Vol. 1, No. 2, pages 86–100. 2005.

[47] Hempel *et al*. "An MRI-Compatible Surgical Robot for Precise Radiological Interventions". *Computer Aided Surgery*. Vol. 8, No. 4, pages 180–191. 2003.

[48] Chen *et al*. "Robotic System for MRI-Guided Focal Laser Ablation in the Prostate". *IEEE/ASME Transactions on Mechatronics*. Vol. 22, No. 1, pages 107–114. 2017.

[49] Su *et al*. "High-field {MRI-compatible} needle placement robot for prostate interventions". *Stud Health Technol Inform*. Vol. 163, pages 623–629. 2011.

[50] Su *et al*. "High-Field MRI-Compatible Needle Placement Robots for Prostate Interventions: Pneumatic and Piezoelectric Approaches". In: *Advances in Robotics and Virtual Reality*. Edited by Gulrez *et al*. Berlin, Heidelberg: Springer Berlin Heidelberg, 2012, pages 3–32.

[51] Tse *et al*. "A 3-DOF MR-Compatible Device for Magic Angle Related In Vivo Experiments". *IEEE/ASME Transactions on Mechatronics*. Vol. 13, No. 3, pages 316–324. 2008.

[52] Yousefi *et al*. "Dynamic Modeling of MRI Compatible Assistant Surgery Robot". In: *13th International Conference on Biomedical Engineering: ICBME 2008*. 2008.

[53] Franco *et al*. "Adaptive control of a master-slave system for teleoperated needle insertion under MRI-guidance". In: *2015 23rd Mediterranean Conference on Control and Automation (MED)*. Pages 61–67. 2015.

[54] Sojoodi Farimani *et al*. *PneuARMM: pneumatically actuated robot for minimally invasive MRI guided interventions*. Pioneers in Health-Care (PiHC) Voucher Proposal. Enschede, The Netherlands, 2018.

[55] Sojoodi Farimani. *Enhanced Reality Panoramic User Interface for Navigation And Documentation of Endoscopic Guided Surgeries (PanoSurg)*. Funded by Pioneers in Health Care Innovation (PiHC) voucher. Enschede, The Netherlands, 2016.

II Principal Studies

2. Introducing PneuAct I

Note: The following content is an adapted version of the paper "Introducing PneuAct: Parametrically Designed MRI-Compatible Pneumatic Stepper Actuator" by F. Sojoodi Farimani and S. Misra, the Proceedings of the IEEE International Conference on Robotics and Automation (ICRA) in May 2018, pages 200–205. ■

Abstract

Pneumatic Stepper Motors (PSMs) are one of the promising alternative actuation methods for motion control in environments where Electromagnetic (EM) motors cannot be used. Due to the lack of Commercially available Off-The-Shelf (COTS) products, researchers working on Magnetic Resonance (MR)-compatible robotics must develop their own pneumatic actuators. This imposes extensive costs and delays on the development process. Additionally, the current solutions are limited in their range of specifications and are challenging to manufacture. In this chapter, proof-of-concept prototypes for a family of parametrically designed, electromagnetically stealth, rotational PSMs are presented. This chapter's main objective is to demonstrate a general-purpose non-EM actuation method, which can be customized and integrated into any robotic platform, regardless of its form factor and design. Customizability, miniaturization, safety, and affordability are critical features of the presented work. The developed prototypes are 3D-printed and contain no sealing, bearing, or lubrication. The motor can be used as a disposable part in surgical applications thanks to the low production cost. Experiments demonstrate the effectiveness of the design in terms of cost-efficiency, versatility, MR compatibility, speed, and performance. To optimize the design and control algorithm, empirical equations are presented describing the response time of a pneumatic system to sequential pressure signals. A rotational speed of 800 RPM, total volume of 4.6 cm^3, and resolution of 3° are some design attributes. The effects of clearance on stick-slip effect and leakage in a 3D printed cylinder-piston are also presented.

2.1 Introduction

EM stepper motors are "*de facto* standard" actuation method for motion control in automation and robotics. However, there are cases where EM motors are not applicable. Medical imaging modalities, such as Magnetic Resonance Imaging (MRI) and Computed Tomography (CT), are examples of such environments [1]. Different industrial and scientific groups have explored alternative actuation methods [2]. Pneumatic power transmission systems and actuators have significant advantages over other alternatives and are considered a promising replacement [3]. In addition to having a high power-to-size ratio, [4], pneumatic actuators are inherently non-EM. Particularly for medical applications, compressed air is easily accessible in the hospital setting. Air does not interfere with imaging processes, and clean air complies with hygienic requirements. Therefore, pneumatic actuation could be the desirable method in image-guided robotic surgery. Despite their advantages, pneumatic systems present complex dynamic behaviors, including compressibility, viscosity, turbulence, throttling, friction, and leakage. As a result, position control of servo-pneumatic actuators, such as cylinder pistons, turbines, and vane motors, is challenging. In contrast, stepper motors can deliver high-precision open-loop motion control with reliable accuracy. A PSM is a volumetric fluidic actuator that can maintain a constant speed, synchronized with the exciting frequency, independent of the external torque and input pressure, within a specific working range, as indicated by its stall curve.

Suzumori *et al*. (1998) reported one of the first implementations of rotational PSMs [5, 6]. The presented motors were not MR-compatible. They also included many parts from different materials, resulting in high manufacturing costs. Taillant *et al*. (2004) [7] were the first group to report a non-EM rotational PSM in a mechanism for image-guided surgery. The concept, called the clock-making principle, resembled a ratcheting socket wrench. The reported actuator was merged into the mechanism and cannot be considered a general-purpose pneumatic motor.

Stoianovici *et al*. (2007) [8] introduced PneuStep, the electromagnetically stealth PSM. PneuStep demonstrated significant performance in terms of resolution and speed-torque characteristics. However, it comprised twenty-five parts made from several materials, imposing high

fabrication costs. Their motor was also not back-drivable, which is essential for a safe surgical robotic system. If an emergency stop occurs, a surgical motorized mechanism with self-locking actuators/joints cannot be easily retracted. A safe surgical mechanism should have a passive mode. In an emergency, the mechanism will be deactivated and turned into a passive tool holder. Therefore, surgeons have complete control over the operation at hand. Sajima *et al*. (2010) [9] reported a novel concept of a PSM similar to a barrel engine. Compared to former designs, their concept had a smaller frontal area and was more affordable. A significant issue with this design is that the parts in the motor are not mechanically coupled. As a result, inaccuracy due to slipping is possible. Chen *et al*. (2014) [10] reported a motor based on the conventional piston and crankshaft concept. This was the first time a conventional concept of an engine was introduced in the field of MR-compatible PSMs. The motor had the advantage of using commercial off-the-shelf products. However, it was rather bulky, not monolithic, and made from many different modules. Chen *et al*. (2015) [11] later reported another motor similar to the mechanism used in push pens. It was the most miniature stepper motor at that moment. However, it was not bidirectional. It was less effective than other motors presented in terms of mechanical performance.

This chapter contributes to the field of pneumatic stepping actuation by providing a novel concept of a parametrically designed, assembly-printed PSM (figure 2.1). The motor is electromagnetically stealth and contains no sealing, bearing, or lubrication. It is safer than the former designs in terms of being back-drivable with adjustable frictional impedance. The travel time of a square pressure signal in a pneumatic tube is studied, and empirical equations are presented. Effects of clearance on the force generated in a 3D-printed cylinder piston are studied. A rigid body model of the system is implemented to compare the calculated and measured torques in a motor. The results of the experiments are used to optimize the design and control system.

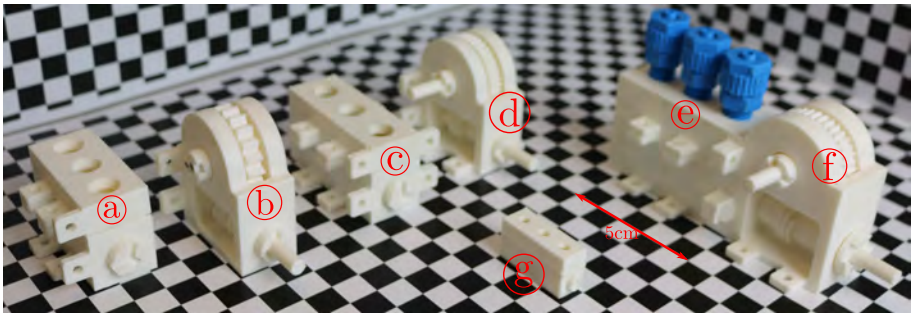

Figure 2.1: 3D printed proof-of-concept prototypes, generated from a single parametric Computer Aided Design (CAD) file with different dimensions. ⓐ Motor with dimension $30 \times 20 \times 46\,\text{mm}^3$. ⓑ Gearhead compatible with ⓐ with a ratio of 1 : 20. ⓒ Motor with dimensions $30 \times 20 \times 55\,\text{mm}^3$ ⓓ Gear-head compatible with ⓒ with a ratio of 1 : 40 ⓔ Motor with dimensions $40 \times 25 \times 40\,\text{mm}^3$ ⓕ Gearhead compatible with ⓔ with a ratio of 1 : 40 . ⓖ Motor with dimensions of $10 \times 15 \times 28\,\text{mm}^3$, with a total volume of $4.6\,\text{cm}^3$. This was the most compact bi-directional rotational Pneumatic Stepper Motor (PSM) at the time.

2.2 Design and prototype

The mechanical composition of any PSM can be broken down into three different elements. The first part converts air pressure into mechanical work. The second part is a linear-to-rotational motion converter. A reduction drive is the last component in a PSM. The reduction drive depends on the user's needs for back-drivability, resolution, size, torque, and speed.

To address the shortcomings in the state-of-the-art, a novel design is presented. The presented concept includes a piston to harness air energy and a scotch yoke mechanism to generate rotational motion. Compared to a normal crankshaft, the scotch yoke mechanism is easier to make, has a more robust structure, and has fewer moving parts. The motor is parametrically designed from the ground up. As a result, the Computer Aided Design (CAD) model can be easily updated automatically by a limited number of driving parameters, such as required torque, pressure, speed, resolution, durability, working range, and size. Motors presented in this chapter are back-drivable with adjustable friction through parametrically controlled clearances. The mechanical design exploits the potential of

additive manufacturing for non-assembly production, reducing costs to a high extent.

A prototype of the proposed design is illustrated in figure 2.2. The motor comprises three different modules printed separately. The main body includes the cylinder ②, the crankshaft ⑤ and three pistons ④$_1$,④$_2$ and ④$_3$. The cylinder-head ① is printed separately to ensure minimum possible clearance between the cylinder and the pistons. The gear-head module ③ includes three parts: structure, worm-gear ③$_2$ and pinion ③$_1$ all printed together. Pistons are arranged linearly. As a result, the motor has a small and customizable frontal area. A schematic of the electro-pneumatic setup is shown in figure 2.3. Three solenoid pneumatic valves create alternating pressure signals to excite each piston. Consequently, the pistons drive the crankshaft through the scotch yoke mechanism.

A worm drive with a sinusoidal tooth profile was prototyped to demonstrate an example of reduction gearing. The gearhead is also parametrically designed. It can be automatically updated based on the motor dimensions and the required resolution, speed, and torque. A ratio of up to 40 has been implemented for the gear-head, increasing the resolution from 120° to 3° in full-pitch drive and from 60° to 1.5° in half-pitch drive. This is smaller than the 3.3° resolution reported by Stoianovici *et al* [8].

Additive manufacturing has been proven to be a promising production method for complex pneumatic motors [13]. A Fused Deposition Modeling® (FDM) 3D printer (STRASYS Fortus 250MC) was used to build all the elements. No sealing, bearing, or lubrication is included in the design. As a result, the motor is highly affordable and can be used as a disposable unit. This expands the motor application to environments such as surgery or the food industry, where hygiene is essential. Airtightness in the motor was achieved through experiments to have the highest input pressure working range (0.15 mm) (figure 2.5). The entire structure of the actuator and the gear head are made of ABSplus™-P430[1]. EM translucency of the motor is demonstrated using MRI tests. Spin Echo and Gradient Echo sequences were applied on a gelatin phantom in three different cases: without the motor, with the motor when it is off, and when the motor is on. No measurable artifacts were observed in the

[1] production-grade thermoplastic by Stratasys® [14]

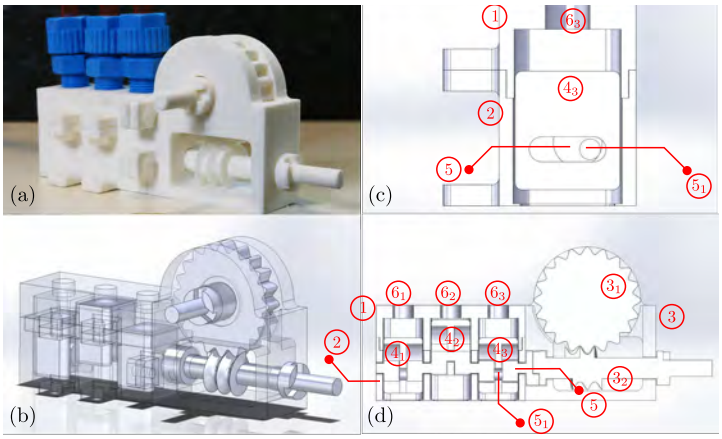

Figure 2.2: (a) A 3D printed prototype of the PneuAct actuator. (b) Components: ① cylinder head, ② cylinder, ③ reduction gear-head, $\textcircled{3_1}$ pinion gear, $\textcircled{3_2}$ worm gear, ④ pistons, ⑤ crankshaft, $\textcircled{6_i}$ $(i = 1, 2, 3)$ inlets. (c) A transverse cross-section of the motor passing through piston $\textcircled{4_3}$ and crank-pin $\textcircled{5_1}$. The crank-pin slides in the horizontal slot in the piston stem, converting the reciprocating motion to rotation (scotch yoke mechanism) (d) A longitudinal cross-section of the motor illustrating the intermeshing mechanism between the crankshaft, the pistons, and the worm drive.

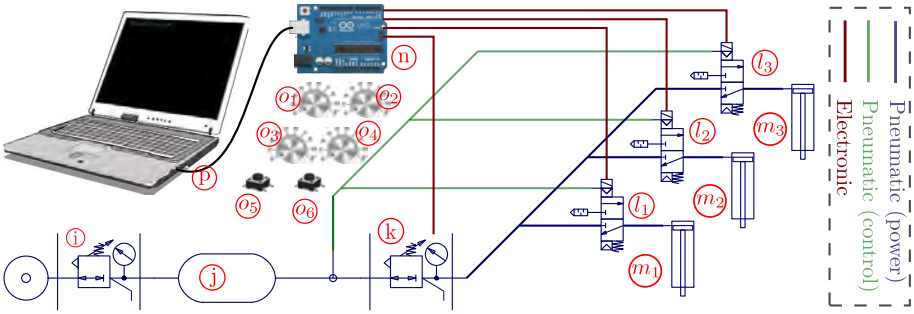

Figure 2.3: A schematic illustration of the motor electro-pneumatic control system. Blue lines and green lines are power and control pneumatic tubes, respectively. Red lines depict the digital electronic wiring. A manual proportional pressure regulator (i) controls the input pressure to the entire system and a reservoir (j) reduces the fluctuations. A digital proportional pressure regulator (k) controls the input pressure to the valves. 3/2 pneumatic solenoid valves (l_1), (l_2) and (l_3) are externally piloted to reduce the effects of pressure change on their performance. Pistons (m), are representations of the pistons inside the motor. Solenoid valves and the digital proportional regulator are controlled via a micro-controller development board, Arduino (n). The motor can be controlled in speed and position control modes via the button (o_5). Potentiometers (o_1), (o_2), (o_3) and (o_4) control parameters: stepping frequency, signal width, position and input pressure, respectively. Button (o_6) controls the direction of the rotation in speed control mode. Serial communication (p) between the Arduino and the computer, through a Universal Serial Bus (USB) interface, is used for data logging, reprogramming the Arduino, and controlling the parameters mentioned.

images, and the SNR is unaffected (figure 2.6). [2].

The successful demonstration of MRI compatibility, combined with the motor's affordability and disposability through 3D printing, represents a significant advancement in the field of medical robotics. These characteristics make PneuAct particularly suitable for MR-guided surgical interventions, where precision, safety, and sterility are paramount considerations. The ability to produce customized, cost-effective actuators that can operate seamlessly within the MRI environment opens new possibilities for developing specialized surgical robotic systems.

[2]Please refer to the video accompanying this publication illustrating more details of design and experiments https://bit.ly/3PrVLNq

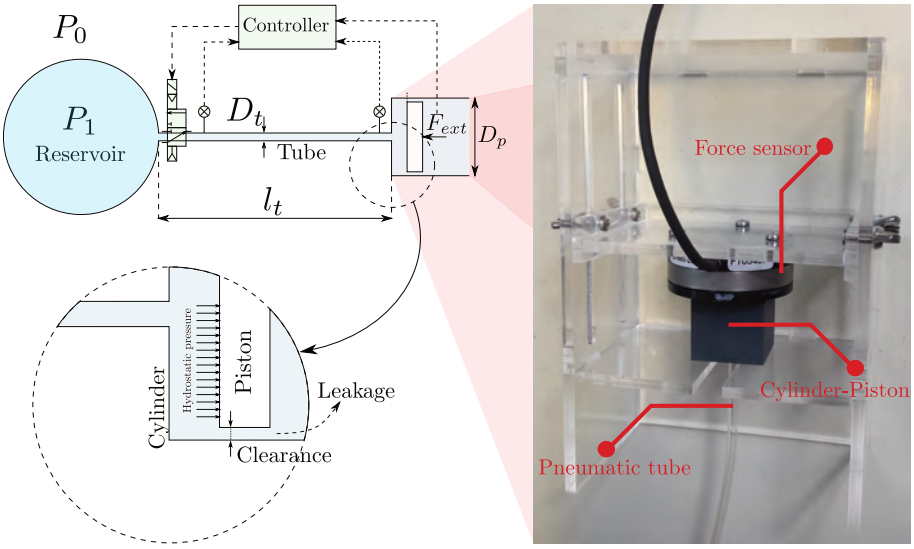

Figure 2.4: Schematics of the experimental setup for measuring the response of a valve, tube, and cylinder piston system to a square wave pressure signal (Force sensor ATI Mini45). P_1 is the pressure of the reservoir, P_0 is the ambient pressure, l_t and D_t are the length and diameter of the tubes respectively, D_p is the diameter of the piston.

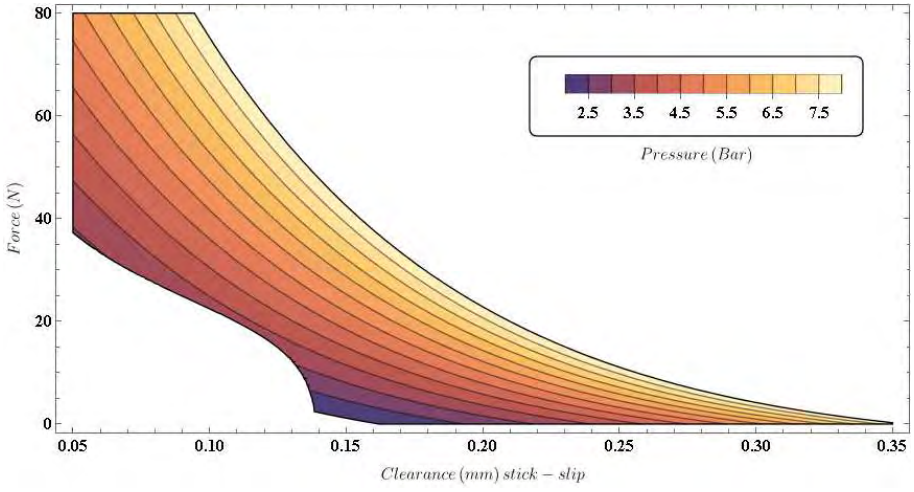

Figure 2.5: An interpolation of measured steady-state force generated in the 3D-printed cylinder-piston illustrated in figure 2.4 with a cross section of $20 \times 20\,\text{mm}^2$. *Experimental data-points available in online repository [12].*

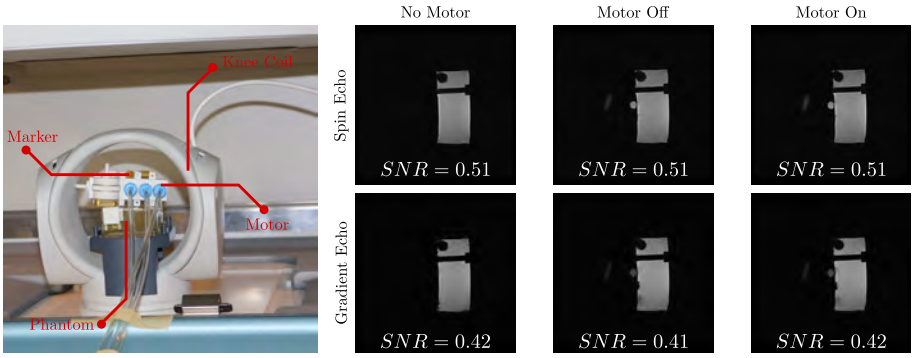

Figure 2.6: Imaging experiments of the motor at different states and modalities, including their respective Signal-to-Noise Ratios (SNRs) in Magnetic Resonance Imaging (MRI) scanner 0.25T G-scan Brio, Esaote SpA (Genoa, Italy). Imaging parameters: Repetition Time (TR) 500 ms, Echo Time (TE) 30 ms, Flip Angle (FA) 90°, Number of Signal Averages (NSA) 1, Field of View (FOV) 20×20 cm, Reconstructed Resolution $0.78 \times 0.78 \times 5$ mm. *Experimental data at GitHub repository [12].*

The integration of additive manufacturing with pneumatic actuation not only addresses the limitations of conventional manufacturing methods but also enables rapid prototyping and iteration of designs. This approach allows for quick validation of different configurations and parametric variations, facilitating the optimization of motor performance for specific applications. The use of FDM technology, in particular, offers a balance between manufacturing precision, material properties, and production costs that is well-suited for both prototype development and potential clinical applications.

2.3 Analysis and results

A mathematical model of the motor is presented to describe its working principle. The power transmission system comprises multiple domains, including pneumatics, rigid body dynamics, and friction. A common approach in the literature is to consider the pneumatics of the system as a reversible and adiabatic (isentropic) thermodynamic process [9]. Additionally, the effects of friction and stick-slip impact have not been included in the models. In this chapter, an experimental approach is presented.

2.3.1 System Pneumatics

Schematics of the experimental setup are illustrated in figure 2.4. Pressure-signal travel time in the tubes and the force generated in a 3D-printed piston cylinder were measured. Tubes with an internal diameter of 4 mm and different lengths were tested under pressure signals with various magnitudes, frequencies, and duty cycles. Pressure sensors (FESTO SPTE-P10R-S6-B-2.5K 571480) at both sides of the tubes measured the magnitude attenuation and phase shift of the pressure wave.

Experiments for different tubes with an internal diameter of 4 mm, and lengths from 1 m to 8 m, under pressures from $2\,Bar$ to $7\,Bar$ were performed. Using curve fitting, an empirical equation was developed to describe the response of the tube to a step signal:

$$P \approx P_1 \left(1 - e^{-0.05e^{-l_t/3}\left(t - \frac{10}{3}e^{l_t/3}\right)}\right), \tag{2.1}$$

, where P and P_1 are the pressure measured by the second sensor (at the end of the tube) and input pressure, and t is time in milliseconds. Results of the experiment are shown in figure 2.8 (a).

To measure the effects of clearance on the force generated in a cylinder-piston, different pistons with various clearances from 0.05 mm up to 0.4 mm were tested. Experiments revealed a stochastic behavior caused by the stick-slip effect. Moreover, the dimensional inaccuracy of the 3D printing method adds to the volatility of the measurements due to the static friction. A residual force after discharge was observed in the force sensor. Both steady-state response and residual force drastically diminish by an increase in clearance. Figure 2.5 shows an interpolation of the experimental data for the output force for different pressures and various clearances. As the graph illustrates, when the clearance is smaller than about 0.2 mm, the stick-slip effect becomes effective, and from there, it drastically increases by decreasing the gap size. An increase in gap size also exponentially decreases the hydrostatic force. The graph shows that a cylinder piston's mechanical performance and working range are directly related. Smaller gaps lead to lower leakage and higher forces, but static friction limits the working pressure range.

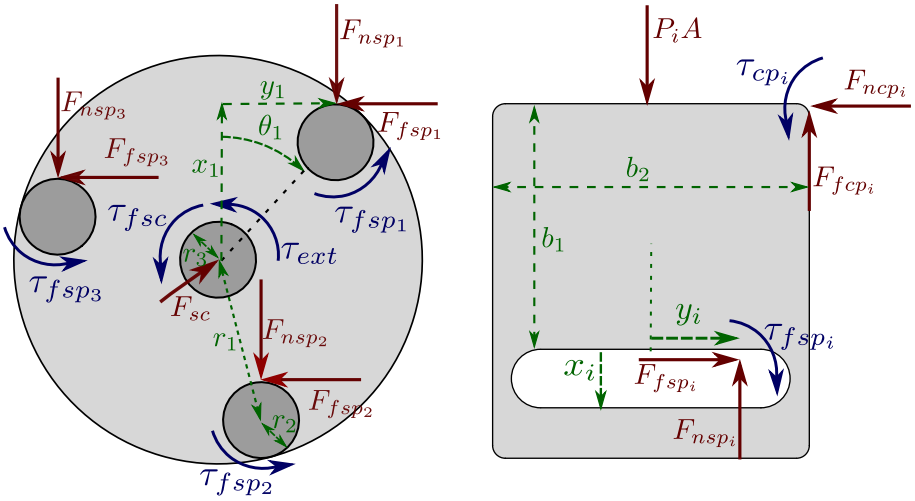

Figure 2.7: Free-body diagram of a piston and the crankshaft. θ_i is the angle between crank-pin i and vertical axis in clockwise direction calculated as $\theta_i = \theta_1 + (i-1)\frac{2\pi}{3}$. τ_{fsc} is the frictional torque between the crankshaft and cylinder, $y_i = r_1 \sin(\theta_i)$ and $x_i = r_1 \cos(\theta_i) + r_2$ are coordinates of the assumed contact points between crank-pins and each piston. F_{nsp_i} is the vertical normal force, and F_{fsp_i} and τ_{fsp_i} are horizontal force and torque due to friction, between the pistons and the crankshaft, $\vec{F}_{sc}$ is the normal force from the cylinder on the crankshaft, F_{ncp_i} and F_{fcp_i} are the normal and friction forces from cylinder on the pistons.

2.3.2 Rigid-body model

A rigid body model of the system is developed to understand the motor's working principle and the interaction between friction and fluidic forces. A free-body motor diagram is shown in figure 2.7, including the interacting forces and torques between the crankshaft, pistons, and cylinder. In an ideal mechanism, the torque exerted by each piston can be calculated by the equation:

$$\tau_i = P_i A_p s_p \sin(\theta_i), \tag{2.2}$$

where A_p is the piston surface area and s_p is the stroke of the piston, $V_c = A_p s_p$ is the maximum volume of each cylinder. Assuming the distribution system is ideal and applies pressure only when the piston

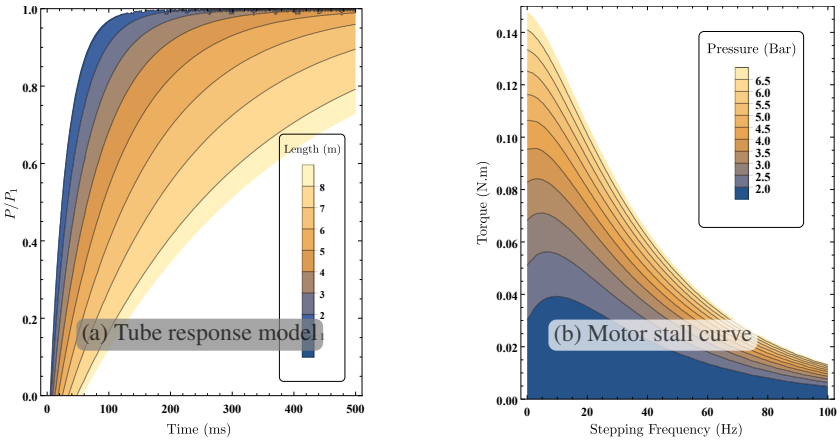

Figure 2.8: (a) Empirical model of the response of tubes with a 4 mm internal diameter and length from 1 m to 8 m to square wave pressure signals from 2 bar to 7 bar. P is the response pressure measured at the end of the tubes (figure 2.4) and P_1 is the input pressure. *Data-points are available at [12].* (b) Stall curve of the motor © gap size: 0.15 mm, piston surface-area: $15 \times 15\,\text{mm}^2$, crankshaft radius: $r_2 = 3\,\text{mm}$ (figure 2.7), Gear-head ratio: 1:40, Input pressure from 1 to 8 Bar, stepping frequency in the (0-100) ms range, pulse-width: 9 ms, Tube length: 3 m and internal diameter: 4 mm. *Experimental data are available in an online repository [12].*

is moving downwards, P_i is a square wave signal. It can be calculated as $P_i = 0.5P_{in}\,(1 + sgn\,(\sin\,(\theta_i)))$, where $sgn(x)$ is the sign function. The average torque during one rotation of the motor can be calculated as:

$$\tilde{\tau} = \frac{1}{2\pi}\int_0^{2\pi}\sum_{i=1}^{1} P_i A_p s_p \sin\,(\theta_i)\,\mathrm{d}\theta_1 = \frac{3V_c P_{in}}{\pi}, \tag{2.3}$$

This is the maximum torque if an ideal motor[3] can convert the total pneumatic energy into mechanical power. However, in reality, leakage and friction dissipate much of the power, as observed during the experiments. Including the effects of friction, considering the planar model of the motor, there are three conservation of momentum equations for each

[3] in the absence of all non-conservative forces such as friction and drag, and no energy loss due to leakage

element. Angular and linear equations of momentum conservation of the crankshaft are:

$$J_s\ddot{\theta}_s = \sum_{i=1}^{3} \tau_i - \tau_{ext} - \tau_{fsc}, \tag{2.4}$$

$$\vec{F}_{sc} = \sum_{i=1}^{3} \begin{pmatrix} F_{nsp_i} \\ F_{fsp_i} \end{pmatrix}, \tag{2.5}$$

where J_c is the angular inertia of the crankshaft, and τ_i is the total torque applied from each piston on the crankshaft, as calculated below:

$$\tau_i = F_{nsp_i} y_i - F_{fsp_i} x_i - \tau_{fsp_i}, \tag{2.6}$$

The conservation of momentum's equations for the pistons are:

$$m_p \ddot{x}_i = P_i A_p - F_{fcp_i} - F_{nsp_i}, \tag{2.7}$$

$$F_{fsp_i} = F_{ncp_i}, \tag{2.8}$$

$$\tau_{fsp_i} + F_{ncp_i}\left(\frac{b_2}{2} - y_i\right) = F_{fsp_i} b_1 - P_i A_p \frac{b2}{2} + \tau_{cp_i}, \tag{2.9}$$

where m_p is the linear inertia of a piston. Figure 2.9 shows the calculated and measured minimum holding torque for the motor © from figure 2.1. The difference between measured and calculated holding torques is mainly due to the simplified Coulomb frictional model.

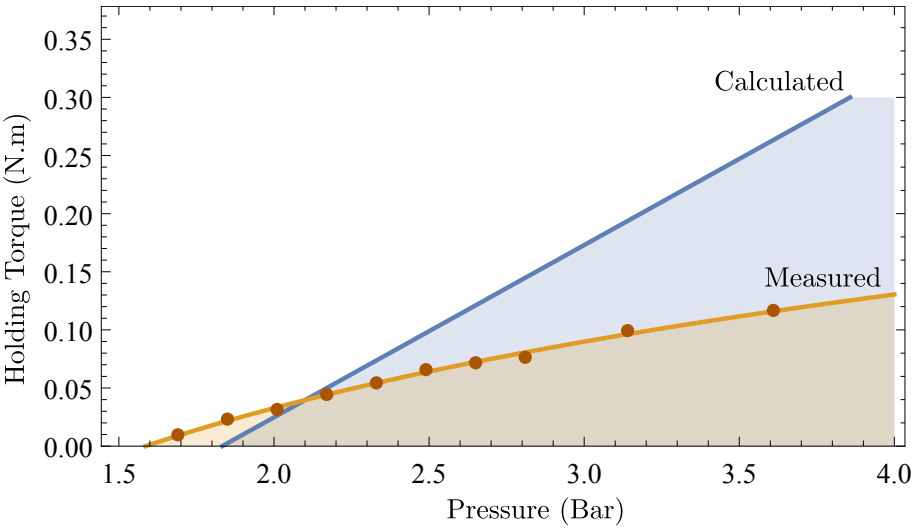

Figure 2.9: Calculated and measured minimum holding torque for the motor © illustrated in figure 2.1, including the logarithmic interpolated trend-line. The measurements demonstrate the relationship between the theoretical predictions and actual performance, with discrepancies primarily attributed to the simplified Coulomb friction model used in calculations. The logarithmic trend suggests a nonlinear relationship between input parameters and holding torque, reflecting the complex interplay of pneumatic forces, mechanical friction, and system geometry. *Experimental data-points are available in an online repository [12].*

2.3.3 Stall Curve

The stall curve indicates the working range of a PSM. The stall curve changes with the input pressure, length, and diameter of the tubes, as well as the duty cycle and frequency of the input pressure waves. For any given Input pressure and frequency, there is a maximum external torque the motor can sustain without skipping any steps. Exceeding this safe torque leads to stochastic behavior due to the stick-slip effect, called ratcheting torque. Similarly, there is a maximum exciting frequency at any given torque and input pressure, called the throttling frequency.

Using dynamometers has been the common approach in literature for torque measurement [8]. However, accurate measurement is challenging due to the abrupt behavior of pneumatic actuation. In this experiment, a pulley mechanism was built, lifting weights to measure the stall torque of the motors. The maximum weight the motor could lift without skipping

any steps was recorded. Different experiments were implemented that measured the effects of pressure input, stepping frequency, speed, pulse width, external torque, length, and diameter of the tubes, as well as the impact of lubrication on motor performance. Figure 2.8 (b) shows the holding torque of the motor ⓒ combined with gear-head ⓓ at different input pressures and stepping frequencies. The surface area of the pistons is $15 \times 15\,\mathrm{mm}^2$ with a gap size of 0.15 mm to achieve the highest pressure range. A constant pulse width of 9 ms was used, the minimum required to activate the valves. Observable non-linearity can be ascribed to leakage and friction. At higher pressures, leakage increases, lowering the mechanical performance of the motor.

As can be seen, the minimum activation pressure slightly improves at higher frequencies, showing the effects of static friction. However, at higher speeds, viscose friction and throttling of the pressure waves in the tubes and valves malfunction, causing the torque to drop rapidly.

2.4 Conclusion

In this chapter, a new paradigm of parametrically designed actuators is introduced. A miniaturized version of the rotational PSM with a total volume of $4.6\,\mathrm{cm}^3$ is presented. PneuAct motors can sustain a no-load-speed of 800 RPM. Using a worm drive, a resolution of 3° at full pitch was achieved. The entire motor and the gear head are 3D-printed with no bearing, sealing, or lubrication. This demonstrates the possibility of making volumetric pneumatic actuators solely with additive manufacturing. The motors are highly affordable and can be used as a disposable part in medical applications. The motors are entirely MRI translucent; no artifacts or distortions were observed in the tests. The motor is back-drivable, providing a safe actuation method for surgical applications, as it can be used as a passive tool-holder in emergencies.

The development of PneuAct represents a step forward in MR-compatible actuation, offering a promising solution for surgical robotics where electromagnetic interference is a concern. The parametric design approach, combined with additive manufacturing capabilities, enables rapid customization and optimization of actuator specifications. The comprehensive characterization of pneumatic system behavior, including the effects of tube dimensions, pressure wave propagation, and clearance-dependent friction, provides valuable insights for future development. These find-

ings, along with the empirical models and experimental results, establish a foundation for optimizing design parameters and control strategies in future iterations, advancing the field of image-guided surgical interventions.

References

[1] Schenck. “The role of magnetic susceptibility in magnetic resonance imaging: MRI magnetic compatibility of the first and second kinds”. *Medical Physics*. Vol. 23, No. 6, pages 815–850. 1996.

[2] Gassert *et al*. “Actuation methods for applications in MR environments”. *Concepts in Magnetic Resonance Part B: Magnetic Resonance Engineering*. Vol. 29B, No. 4, pages 191–209. 2006.

[3] Chinzei *et al*. “MR Compatibility of Mechatronic Devices: Design Criteria”. In: *Medical Image Computing and Computer-Assisted Intervention – MICCAI’99*. Pages 1020–1030. 1999.

[4] Lazar *et al*. *Pneumatic actuating systems for automatic equipment: structure and design*. Crc Press, 2016.

[5] Suzumori *et al*. “A direct-drive pneumatic stepping motor for robots: designs for pipe-inspection microrobots and for human-care robots”. In: *Proc. IEEE Int. Conf. on Robotics and Automation (ICRA)*. Vol. 4, pages 3047–3052. 1998.

[6] Suzumori *et al*. “Pneumatic direct-drive stepping motor for robots”. In: *IEEE/RSJ International Conference on Intelligent Robots and Systems*. Vol. 2, pages 2031–2036. 2002.

[7] Taillant *et al*. “CT and MR Compatible Light Puncture Robot: Architectural Design and First Experiments”. In: *Medical Image Computing and Computer-Assisted Intervention – MICCAI 2004: 7th International Conference, Saint-Malo, France, September 26-29, 2004. Proceedings, Part II*. Edited by Barillot *et al*. Berlin, Heidelberg: Springer, 2004, pages 145–152.

[8] Stoianovici *et al*. “A New Type of Motor: Pneumatic Step Motor”. *IEEE/ASME Transaction on Mechatronics*. Vol. 12, No. 1, pages 98–106. 2007.

[9] Sajima *et al*. “Two-DOF non-metal manipulator with pneumatic stepping actuators for needle puncturing inside open-type MRI”. In: *World Automation Congress*. Pages 1–6. 2010.

[10] Chen *et al*. “An MR-Conditional High-Torque Pneumatic Stepper Motor for MRI-Guided and Robot-Assisted Intervention”. *Annals of Biomedical Engineering*. Vol. 42, No. 9, pages 1823–1833. 2014.

[11] Chen *et al*. "A 10-mm MR-Conditional Unidirectional Pneumatic Stepper Motor". *IEEE/ASME Transaction on Mechatronics*. Vol. 20, No. 2, pages 782–788. 2015.

[12] *GitHub repository for experimental data-points*. https://goo.gl/9o2p6u.

[13] Wei *et al*. "Novel Design and 3D Printing of Nonassembly Controllable Pneumatic Robots". *IEEE/ASME Transactions on Mechatronics*. Vol. 21, No. 2, pages 649–659. 2016.

[14] *ABSPlus-P430 for Fortus 3D Production Systems*. STRATASYS.

3. Friction of FDM Surfaces

Note: The following content is an adapted version of the paper "Frictional Characteristics of Fusion Deposition Modeling (FDM) Manufactured Surfaces" by F. Sojoodi Farimani, M. de Rooij, E. Hekman, and S. Misra, Rapid Prototyping Journal (RPJ), volume 26, issue number 6, pages 1095–1102, 12 May 2020. ■

Abstract

Additive Manufacturing (AM) is a promising alternative to conventional production methods, providing significant geometrical and topological freedom during design. However, frictional characteristics of AM surfaces are yet to be fully explored, making the control and manufacturing of precise assembly-manufactured mechanisms challenging. This chapter investigates the tribological behavior of Fused Deposition Modeling® (FDM) manufactured surfaces and evaluates the accuracy of existing mathematical models such as Coulomb-Amontons (CA), Tabor-Bowden (TB), and variations of the Hertz Contact model against empirical data.

Experiments measure friction between two flat FDM surfaces at different speeds, normal forces, and surface configurations, including the relative direction of printing stripes, sliding direction, and surface area. Results show that friction between FDM planes is linearly proportional to the normal force. However, in contrast to viscous frictional models, friction reduces asymptotically at higher speeds, attributed to the transition from harmonic to chaotic vibrations. The phase shift is investigated through spectral analysis, with dominant frequencies presented at different pulling speeds, normal forces, and surface areas.

This study contributes to the field by developing theoretical tribological models for the specific topography of FDM-manufactured surfaces and providing comprehensive experimental validation. The findings enable better predictive and model-based control algorithms for fully AM-manufactured mechanisms, particularly in applications requiring precise motion control. The results demonstrate that FDM-manufactured surfaces should be considered among textured surfaces, as conventional friction models do not adequately represent their frictional behavior. ■

3.1 Introduction

AM technology [also known as 3D printing [1]] enables developers to design parts with higher topological and geometric complexities. Some concave or hollow geometries are not feasible by conventional machining, hereafter referred to as Subtractive Manufacturing (SM). AM entails lower costs and lead time for low-volume and customized production. Being a direct digital manufacturing method, AM also offers a faster research and development process for innovative industries[2]. Non-assembly production is also one of the unique features of AM where a complete integrated functional mechanism, with embedded moving joints, can be printed without requiring further assembly (also known as assembly printing). AM is experiencing a major transformation from demonstrative/rapid prototyping to functional manufacturing, with rapid iterations and design improvements possible, where the parts are being directly used as/in the actual products [3]. Therefore, the final properties of the printed parts, including geometric, mechanical, tribological, electromagnetic, and thermal characteristics, should be better understood. Medical, food, space, and do-it-yourself (DIY) industries are some of the application areas where AM technology is already deployed or significant development is undergoing [4–6].

Various AM methods are available, with various price choices for hobbyists and professionals. FDM, also known as material extrusion [1], is one of the most popular commercially available AM methods. FDM machines deposit stripes of melted thermoplastics, such as Acrylonitrile Butadiene Styrene (ABS) and PolyLactic Acid (PLA), to form a 3D object. FDM parts are affordable and have good mechanical performance, including strength and durability, compared to other AM methods. Particularly, FDM-ABS parts have the advantage of being environmentally friendly thanks to the material's recyclability. Besides, they present other properties, such as being chemically inert and self-lubricating. These make FDM-ABS ideal for tribological applications and manufacturing of disposable parts, for example, in surgical applications [3, 7].[1]

One of the primary drawbacks of AM parts in comparison to SM is the fact that they bear rougher surface topographies and nonuniformly distorted geometries, as demonstrated in figure 3.1 [8–11]. This complicates

[1] In the context of this research the primary interest is in the surgical applications of the results, including disposable components for robotically assisted interventions

manufacturing airtight fluidic systems (i.e., hydraulic and pneumatic) and precise mechanisms with moving joints (e.g., robotics). Friction reduces the mechanical systems' controllability and accuracy/precision and adversely affects their energy efficiency. Understanding the frictional behavior of the AM surfaces is crucial to producing and controlling fully 3D-printed mechanisms (e.g., assembly printing).

The dry friction phenomena can present chaotic behavior, and without experiments, it is challenging to estimate it in a specific system [12–16]. A plethora of research has been done on the friction of polymers, and different frictional coefficients have been reported: for steel on ABS with presumably smooth surfaces, static 0.35 and dynamic 0.30 [17], static 0.2 and dynamic 0.15 [18], average dynamic 0.376 [19]. Difallah *et al*. (2012) [20] reported the effects of additives on the mechanical and wear properties of ABS. Leacock *et al*. (2014) [21] studied the effect of sliding distance on frictional coefficients between FDM printed ABS surface and smooth titanium using the strip pull-friction-test at different normal pressures (2.36-7.08) MPa, speeds (50-250) mm/min and sliding directions (perpendicular to stripes and 45°). They showed that the friction increases by sliding distance, reaching a maximum when surface ripples are worn out. Gurrala *et al*. (2014) [22] investigated the effect of load and sliding speed on pin-on-disk friction of FDM-ABS parts, observing an increase in friction by wear. Dawoud *et al*. (2015) [23] explored the effects of 3D printing parameters such as gap and scaffolding angle on wear. Boparai *et al*. (2016) [24] investigated the effects of load and wear on friction in a pin-on-disk apparatus. Perepelkina *et al*. (2017) [25] studied the effect of filling factor, temperature, and wear on the friction of FDM printer tribopairs. Beg *et al*. (2017) [26] studied the abrasive properties of FDM-ABS parts. Farstad *et al*. (2017) [27] investigated the friction of printed thermoplastic elastomers on smooth surfaces. Sood *et al*. (2010) developed heuristic methods (i.e., artificial neural networks) to predict the effect of printing parameters on precision, accuracy, and tribomechanical properties of AM parts [28–30].

Nevertheless, the tribological characteristics of 3D-printed FDM-ABS surfaces have yet to be fully understood. Former studies are merely experimental, not considering the surface topography of the FDM parts. They have been mostly performed between FDM/ABS/Polymers and other materials. Therefore, the results are not necessarily extendable

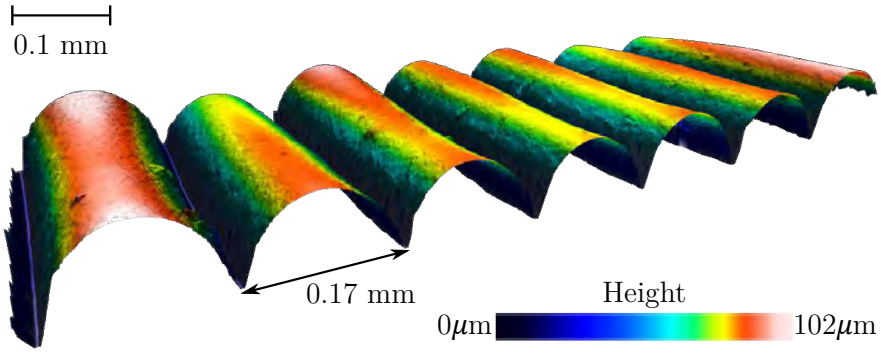

Figure 3.1: Surface magnification of a 3D printed part made of ABSplus™-P430, using Stratasys® Fortus®-250MC. Sensofar® optical profilometer has been used to scan the surface topography. The measurement shows that the surface of the 3D printed parts comprises a series of parallel cylinders with a diameter of approximately 0.17 mm.

to the frictional behavior of fully 3D-printed mechanisms. This study explores the friction between two sets of identical flat surfaces made of FDM-manufactured ABS using Stratasys® (Rehovot, Israel) Fortus® 250MC. A Zwick® tensile machine (ZwickRoell®, GA, USA) measures the pulling force against displacement, experimenting with effects of normal force, printing direction, sliding direction (as illustrated in figure 3.2), surface area, and sliding speed on friction. Experiments for validation and parameter identification follow mathematical modeling for surface topography and friction. Eventually, the theoretical models are validated against the empirical data.

The friction force between two flat surfaces depends on various factors such as normal contact pressure, lubrication, dwell time, sliding speed, and surface topography. Different models have been developed for friction, prominently CA model, which describes the friction force F_f between two dry surfaces with random roughness as linearly proportional to the normal force F_N:

$$F_f = \mu_f F_N \,, \tag{3.1}$$

where μ_f is the Coefficient of Friction (CoF). In equation (3.1) the μ_f is dimensionless if both F_N and F_f carry identical dimensions (N). Bowden

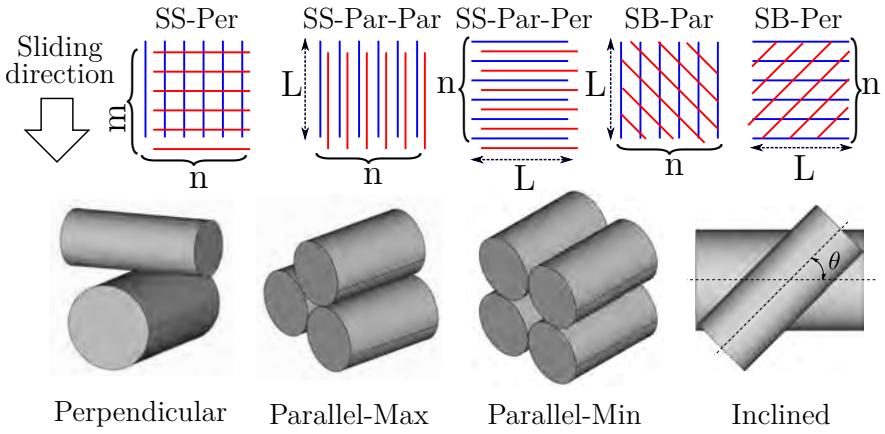

Figure 3.2: Different sliding scenarios considering the printing surface (bottom/top B and side S) and sliding directions (parallel Par and perpendicular Per) were experimented with. Based on the alignment of the two surfaces, the printing stripes can be parallel (SS-Par), perpendicular (SS-Per), or inclined (SB) with an angle of $\theta = 45°$. In SS-Par alignment, two different contact scenarios should be considered where each cylinder is in contact with one (Parallel-Min) or two (Parallel-Max) cylinders from the adjacent surface.

et al. (1943) [31] showed that the CA-CoF at high normal pressures [2] , where surface asperities experience plastic deformation, is proportional to yield shear stress τ_y (MPa) divided by hardness H in Brinell scale (BHN), of the softer material:

$$\mu_f \approx \frac{\tau_y}{H}. \tag{3.2}$$

A yield shear stress of (30-45) MPa and a Brinell hardness of (95-100) MPa have been reported for ABS [18, 19, 32, 33], therefore an approximate CA-CoF of 0.3-0.45 is to be expected. Although the CA model is simple and practical, it does not represent the effects of surface topography, contact area, and sliding speed.

[2] A tensile strength of 37 MPa has been reported for ABSplus™-P430 by Stratasys® [32]

3.1.1 Surface topography

The binomial TB equation is one of the primary models describing the effects of surface topography, normal force, and mechanical properties of the materials on friction [34–37]. The TB model divides the friction force into two distinct parts:

$$F_f = F_a + F_m\,, \tag{3.3}$$

where F_a and F_m are the adhesive and mechanical components, respectively. F_m is a collective term including several forces such as internal hysteresis of the materials due to the visco-elastic/plastic deformation (i.e., cohesion), as well as abrasion of the contact surfaces (also referred to as wear, grooving, scratching, or plowing/ploughing in the literature). Practically plowing is considered negligible if the difference between the hardness of two surfaces is less than 20% [38]. This applies to our case, considering that adjacent surfaces are identical. The adhesive force F_a (N) is mainly due to the intermolecular/chemical interactions between the two contacting surfaces. Adhesion has been described as:

$$F_a = \tau_s A_r\,, \tag{3.4}$$

where A_r (m^2) is the real contact area, and τ_s (Pa) is the shear adhesion strength. In the following sections, different models describing these two terms are elaborated:

Contact area

The actual contact area A_r for rough surfaces is significantly smaller than the apparent surface area A_a. For perfectly random topographies, the ratio of real to apparent contact areas is linearly proportional to the normal force F_N:

$$A_r \propto k F_N A_a^n\,, \tag{3.5}$$

where k represents the elastic behavior of the contact or hardness of the softer material if contact pressure is above its plastic/yield threshold [39].

However, the real contact area for defined topographies should be calculated analytically using variations of the Hertz contact model. It is known that parts made by FDM have a parabolic surface profile [10, 11]. As a confirmation, figure 3.1 also shows a magnification of the surfaces made by a Fortus®-250MC 3D printer, using a Sensofar® (Barcelona, Spain) microscope (optical profilometer for non-contact 3D metrology). It can be seen that the 3D printed surface comprises parallel cylindrical stripes with diameters of 0.17 mm. The observation agrees with the minimum layering thickness used for printing, which was also reported for this particular 3D printer. The Stratasys® Insight® slicer has been used to generate the tool path. Default settings of the Stratasys® Insight® slicer have been used as detailed in table 3.1.

Parameter	Value
Part interior style	Sparse-high density
Visible surface style	Enhanced
Support style	SMART
Model material	ABS-P430
Support material	ABS-SR30
Slice height	0.1778 mm
Merge open curve tolerance	0.1270 mm
Curve filtering tolerance	0.0102 mm
Contour width	0.3556 mm
Enhanced visible rasters	0.3556 mm
Enhanced internal rasters	0.4572 mm

Table 3.1: 3D Printing Parameters used in the Stratasys® Insight® slicer software for manufacturing test specimens. These parameters significantly influence the surface characteristics and mechanical properties of the printed parts, particularly the slice height and raster settings which directly affect the surface topography.

The Fortus® machine prints parts with horizontally aligned stripes on the side walls. By default, the printer also fills internal cavities with stripes at 45° angle, leading to stripes on bottom surfaces with the same angle.

Since printed parts have two different surfaces (top/bottom and side), various sliding scenarios exist (figure 3.2).

For example, two side surfaces can have parallel (SS-Par) or perpendicular (SS-Per) alignments. When parallel, the relative motion can be alongside the cylinders' direction (SS-Par-Par) or perpendicular (SS-Par-Per). Therefore, there are three different possibilities for side-side (SS) configuration. In a parallel configuration, each cylinder can be either in contact with a single cylinder from the opposite side (Par-Min) or with two (Par-Max) (figure 3.2). Therefore, four different contact models (Par-Min, Par-Max, Perpendicular, and Inclined) are considered depending on the relative alignment of the cylinders.
The contacts between individual pairs of stripes can be calculated from variants of the Hertz model if the deformations stay within the elastic range. Other assumptions of the Hertzian contact models are that the effect of adhesion on contact is negligible and the diameter of the contact area compared to the diameter of the main objects is insignificant. For identical parallel cylinders (SS-Par) the Radzimovsky model [40–43], describes the width of contact a_c (m) as:

$$a_c = 2.15\sqrt{\frac{F_N^* R}{LE}}, \tag{3.6}$$

where F_N^* (N) is the total contact force across one pair of cylinders with a radius of R (m), and E (Pa) is the elastic modulus, and L (m) is the length of the contact alongside the cylinder's axis. For the special case of identical perpendicular cylinders, the contact can be considered circular, calculated from the contact between a plane and a sphere of the same radius [44, 45]. From the Hertz-Goldsmith model, the radius r_c (m) of circular contact between a sphere and a plane of the same material is:

$$r_c = \left(\frac{3F_N^* R}{4E}\right)^{\frac{1}{3}}. \tag{3.7}$$

For inclined cylinders, the contact area is elliptic [46, 47]. However, for simplicity in the case of identical cylinders with an angle of $\theta = 45°$, it can be approximated with the circular contact between a plane and a sphere with an average radius of $R_e \approx \sqrt{2}R$. For parallel alignments, the

total real and apparent contact areas can be calculated from the geometry of the cases:

$$Min: \begin{cases} A_r = na_cL \\ A_a = 2nRL \end{cases}, Max: \begin{cases} A_r = 2na_cL \\ A_a = 2nRL \end{cases} \tag{3.8}$$

where n is the number of rows, and L is the length of the cylinders. In the perpendicular configuration, the contact areas are:

$$\begin{cases} A_r = nm\pi r_c^2 \\ A_a = nm4R^2 \end{cases}, \tag{3.9}$$

where nm is the number of rows$\times$columns, including all contact points. For inclined configuration, the approximate number of contacts can be calculated from:

$$n_e \approx \frac{nL\sin\theta}{2R}, \tag{3.10}$$

and contact areas can be calculated consequently as:

$$\begin{cases} A_r \approx n_e\pi r_c^2 \\ A_a = 2nRL \end{cases}. \tag{3.11}$$

Considering that equations (3.6) and (3.7) represent individual contacts, extending them to the whole contact surface and combining them with equations (3.8), (3.9) and (3.11) yields:

$$A_r = k_1\sqrt{\frac{F_N}{E}}A_a^{\frac{1}{2}}, \tag{3.12}$$

for parallel alignments, where $k_1 = 3.04$ for Min and $k_1 = 2.31$ for Max contact scenarios, and

$$A_r = k_2\left(\frac{F_N}{E}\right)^{\frac{2}{3}}A_a^{\frac{1}{3}}, \tag{3.13}$$

for perpendicular ($k_2 = 1.63$) and for inclined ($k_2 = 1.83$) surface configurations. In the above equations, F_N is the total normal force between the two surfaces, which is distributed uniformly across the contact area. Also, the k_* coefficients are dimensionless.

Adhesion

Amuzu *et al*. (1977) [48] have shown that the adhesion shear strength in polymers is close to their bulk shear strength. Hence, an adhesive shear strength τ_s in the same order as (15-27) MPa for ABS is to be expected. However, Bowden *et al*. (1954) [34] have proposed a linear relationship to account for the effect of contact pressure:

$$\tau_s = \tau_0 + \alpha P_m \,, \tag{3.14}$$

where $P_m = F_N/A_r$ (Pa) is the mean effective contact stress and α is the dimensionless piezo coefficient of adhesion. Integrating equations (3.3), (3.4) and (3.14) yields:

$$F_f = \tau_0 A_r + \alpha F_N \,, \tag{3.15}$$

and replacing A_r from equations (3.12) and (3.13) will describe the friction force versus normal force and apparent contact area for different surface configurations according to the TB model.

3.1.2 Sliding speed

A combination of different underlying phenomena determines dynamic friction in the system, including viscosity, creep, and morphological vibrations. The self-lubricating characteristics of polymers can manifest themselves as viscosity at certain conditions, wherein the presence of liquid film in the Stribeck model could be used [49–52]. Sliding speed also affects friction through vertical vibrations during the stick-slip effect. For instance, Al-Bender *et al*. (2004) [53] extended the B.Sc. (1929) [54] model to macro-scale periodical surfaces. Furthermore, sliding speed can also affect the dwell time (relaxation), consequentially altering friction. Kato *et al*. (1972) [55] have described the effect of dwell-time on friction, showing that at a low sliding speed, more adhesive

bonds are developed between the asperities of the contacting surfaces, increasing adhesive force. The actual contact area increases over time due to creep, decreasing the coefficient of friction at higher speeds [56].

3.2 Experiments

A series of experiments are implemented to investigate the validity of the developed mathematical models. Frictional behavior between two 3D printed parts (a box and a plate) is studied (figure 3.3). Different contact configurations are considered, including the effects of surface area, printing direction (top/bottom and side), and sliding directions with regard to the printed strips (parallel, perpendicular, and inclined).

As shown in figure 3.3, a Zwick® tensile machine is used to pull the box on top of the plate and to measure the sliding force versus jaw displacement. Experiments are repeated for different pulling speeds $(5\text{-}1800)\,\mathrm{mm/min}$, normal forces $(40\text{-}250)\,\mathrm{g}$, different surface configurations (bottom/side-parallel/perpendicular) and surface areas $A_a = (900 - 2500)\,\mathrm{mm}^2$. Raw measurement data can be found at the provided repository [57].

Figure 3.4 shows a sample measurement for a surface area of $0.0025\,\mathrm{m}^2$, normal force of $232\,\mathrm{g}$ and pulling speed of $300\,\mathrm{mm/min}$. It can be seen that when the pulling process starts, the measured force rises first, while energy is stored in the adhesive bonds of the contact surfaces, as well as the cable. At some point, the intermolecular conjunctions between the contact surfaces collapse, and a phase shift from static to kinetic friction happens. The stick-slip effect in the kinetic phase causes an oscillatory force measurement.

Measured data are analyzed to find the maximum global force (i.e., breakaway static friction) and the average of local maxima (representing kinetic friction), average local minima, and periodicity of the oscillations during the kinetic phase. Three different spectral analysis methods are developed to calculate the periodicity and local extremes, including the Fourier Transform, Autocorrelation, and manual filtering [57].

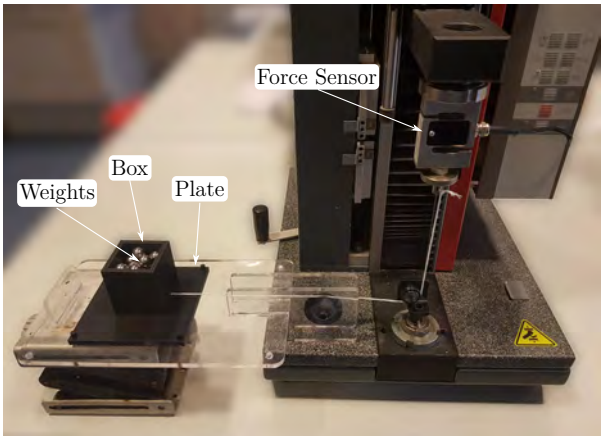

Figure 3.3: A Zwick® tensile machine is used to measure friction force between the two 3D printed surfaces. A flat square surface with a side length of 10 cm is fixed to the ground while a box with different surface areas is being pulled on top of it. The normal force between the two surfaces is controlled by changing the weights inside the box. The force sensor attached to the machine measures the force while the position is also being recorded simultaneously.

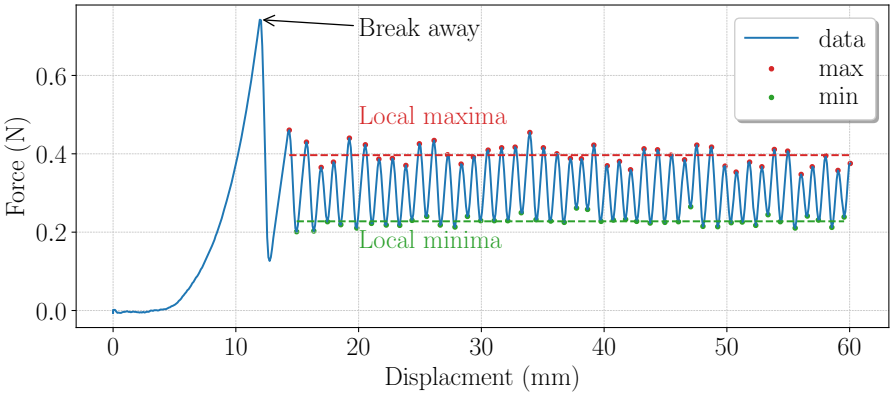

Figure 3.4: Force versus displacement (of the force-cell) measurements by the Zwick® tensile machine, for a normal force of 232 g, a pulling speed of 300 mm/min, a square apparent surface area of 0.0025 m^2, between the bottom surface and side surface, with rows parallel to the direction of sliding (BS-Par).

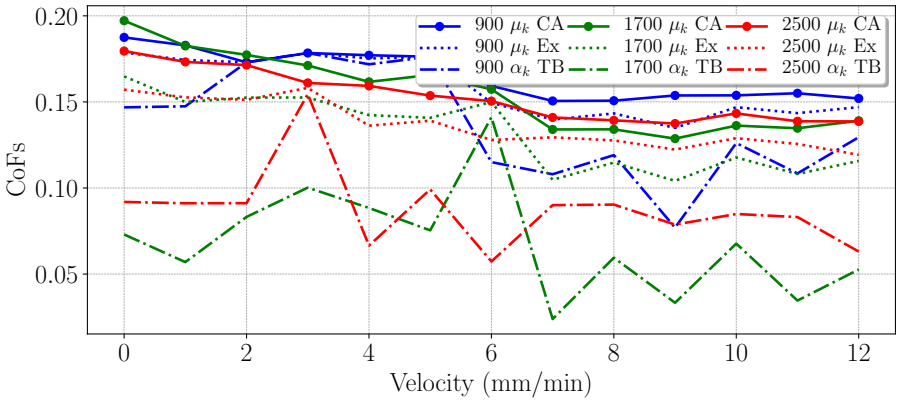

Figure 3.5: Coefficients of kinematic friction μ_k for the Coulomb-Amontons (CA) and Ex models, and piezo coefficient of adhesion α_k from the Tabor-Bowden (TB) model for SS-Per surface configuration at different pulling speeds (5-1800) mm/min and apparent surface areas $A_a = (900 - 2500)\,\text{mm}^2$. It can be seen that the TB model leads to incoherent results at different speeds, and the effect of apparent surface area is noticeable but non-monotonic.

3.3 Analysis

As expected, it is observed that normal force is the dominant influencing factor in both static and kinetic friction forces. However, attempts to fit the TB models lead to incoherent coefficients at different pulling speeds (figure 3.5). It can be seen that the surface area has a noticeable but non-monotonic effect on the force of friction. One interpretation could be that the Hertz models do not represent these surfaces' contact behavior. An extended CA model with an offset (F_0) representing an initial surface adhesion appears to be the most reliable representation of the measurements:

$$F_f = \mu F_N + F_0 \,. \tag{3.16}$$

Figure 3.6 demonstrates the linearity of the correlation between friction-normal forces, including linear interpolations and error bands at different sliding speeds. The average static and kinetic friction coefficients for different surface configurations were calculated and are presented in table 3.2, showing consistent patterns across all test conditions.

Surface configurations (alignment and sliding direction) are shown to be the second influencing parameter. SS-Par-Per configuration shows the highest friction forces followed by SS-Par-Par and SS-Per. The fact that SS-Par-Per presents higher friction forces than SS-Par-Par while SS-Par-Per has a smaller contact area can be attributed to the formerly neglected deformation factor F_m from the TB model. In contrast to the viscous model, at higher speeds, an asymptotic decline in static and kinetic friction forces is observed. For example, figure 3.7 shows average kinetic friction forces for different masses versus speed for BS-Par configuration with a $0.0025\,\mathrm{m}^2$ surface area.

As mentioned, this behavior can be assigned to vertical wobbling and reduction of dwell time. Similar behaviors have been reported for textured surfaces [58, 59]. Figure 3.8 shows the dominant frequency of the slip-stick phase for the previous model at different speeds and normal forces. It was also observed that the oscillatory motion becomes less harmonic at pulling speeds higher than $200\,\mathrm{mm/min}$ while spending more time sliding during each oscillation. Therefore, it can decrease dwell time significantly.

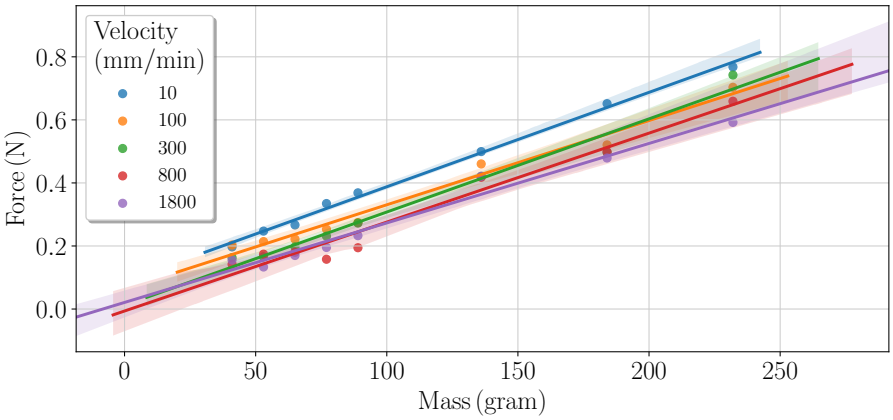

Figure 3.6: Static friction force versus normal force at different speeds for the measurements of figure 3.5. The extended Coulomb-Amontons (CA) friction model with an initial adhesive force F_0 describes the linear relationship between the friction and normal force.

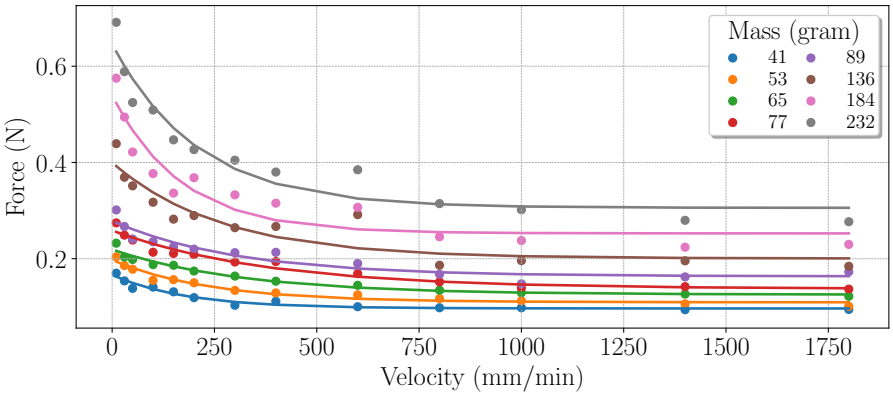

Figure 3.7: Average of maximum friction forces during the kinetic phase versus speed in addition to the interpolated graphs. Kinetic friction force decreases at higher pulling speeds, asymptotically reaching a minimum friction force.

Surface	μ_s	F_{0_s} (N)	μ_k	F_{0_k} (N)
SS-Par-Per	0.291	0.089	0.184	0.063
SS-Par-Par	0.245	0.073	0.157	0.048
SS-Per	0.220	0.048	0.143	0.026
Average	0.253	0.072	0.158	0.047

Table 3.2: Friction coefficients and forces for various surface configurations, showing static (μ_s) and kinetic (μ_k) friction coefficients along with their corresponding initial adhesion forces (F_{0_s} and F_{0_k}). The configurations include Side-Side Parallel-Perpendicular (SS-Par-Per), Side-Side Parallel-Parallel (SS-Par-Par), and Side-Side Perpendicular (SS-Per) alignments. The results demonstrate that the SS-Par-Per configuration exhibits the highest friction coefficients and initial adhesion forces, while the SS-Per configuration shows the lowest values across all measurements.

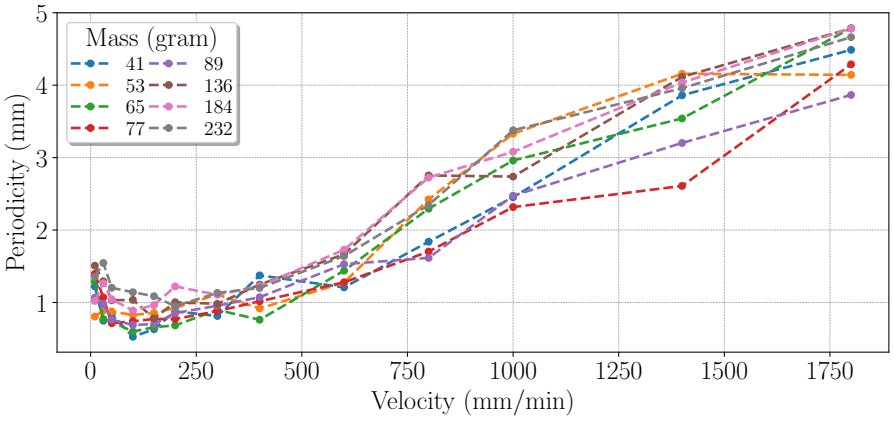

Figure 3.8: Average periodicity (dominant frequency of the oscillation during the kinetic phase) versus pulling speed for different normal forces: the average dominant frequency slightly decreases from zero to 200 mm/min and then the oscillatory motion becomes less harmonic.

3.4 Conclusion

This study investigated the frictional behavior of surfaces made by Stratasys® Fortus®-250mc FDM printer. Effects of normal force, pulling speed, surface configuration, and contact area on static and kinetic friction were investigated. Mathematical models were developed and compared against empirical data. Results reiterated the chaotic nature of the friction phenomenon, showing it reflects drastically toward changes in the initial and boundary conditions. Some major assumptions of our model are the simplified geometrical shapes, linear elastic behavior, small contact area compared to the radius (Hertzian assumption), and no adhesion or other surface forces (Hertzian assumption).

It was shown that the combination of the Hertz contact model and the TB frictional model does not represent the effect of surface topography and normal force on static and kinematic friction forces. A modified CA model with an initial force representing the adhesive effect between the surfaces appears to be the most coherent description. It is also demonstrated that the pulling speed significantly affects the friction force reduction, in contrast to the viscous model. Spectral analyses of the kinetic oscillations revealed a chaotic phase shift at certain pulling speeds. This can be described by vertical micro-vibrations affecting the dwell time and, therefore, decreasing the adhesion between the surfaces. Further research, including a wider range of normal force and surface areas, is required to investigate the validity of this observation. It can be concluded that the FDM-manufactured surfaces should be considered among textured surfaces since conventional friction models such as TB and Stribeck do not represent their frictional behavior.

This research provides critical insights into the complex and multifaceted nature of frictional behavior exhibited by FDM-manufactured surfaces. Through rigorous investigation and analysis, the limitations of conventional friction models in accurately representing the unique characteristics of these surfaces were illuminated. The study underscores the necessity of adopting modified models that account for adhesive effects and the impact of micro-vibrations on frictional forces. These findings not only challenge existing paradigms but also open new avenues for the design and optimization of 3D-printed components across various applications. The frictional properties of FDM surfaces are significantly influenced by their textured nature and operational conditions, necessi-

tating a reevaluation of standard models to achieve precise control and predictability in manufacturing processes.

References

[1] ASTM-F2792-12. *Standard Terminology for Additive Manufacturing Technologies*. Standard. West Conshohocken, PA: ASTM International, 2012.

[2] Chua *et al*. *Rapid Prototyping: Principles and Applications*. 3rd. WORLD SCIENTIFIC, 2010.

[3] Sojoodi Farimani *et al*. "Introducing PneuAct: Parametrically-Designed MRI-Compatible Pneumatic Stepper Actuator". In: *Proc. IEEE Int. Conf. on Robotics and Automation (ICRA)*. Pages 200–205. 2018.

[4] Govender *et al*. "Therapy for the individual: Towards patient integration into the manufacturing and provision of pharmaceuticals". *European Journal of Pharmaceutics and Biopharmaceutics*. Vol. 149, pages 58–76. 2020.

[5] Attaran. "The rise of 3-D printing: The advantages of additive manufacturing over traditional manufacturing". *Business Horizons*. Vol. 60, No. 5, pages 677–688. 2017.

[6] Fox. "Paradigm shift: do-it-yourself (DIY) invention and production of physical goods for use or sale". *Journal of Manufacturing Technology Management*. Vol. 24, No. 2, pages 218–234. 2013.

[7] Sojoodi Farimani *et al*. "PneuAct-II: Hybrid Manufactured Electromagnetically Stealth Pneumatic Stepper Actuator". *IEEE Robotics and Automation Letters*. Vol. 5, No. 2, pages 3588–3593. 2020.

[8] Pérez. "Analysis of the surface roughness and dimensional accuracy capability of fused deposition modelling processes". *International Journal of Production Research*. Vol. 40, No. 12, pages 2865–2881. 2002.

[9] Nourghassemi. "Surface roughness estimation for FDM systems". PhD thesis. Ryerson University, Toronto, ON, Canada, 2011.

[10] Taufik *et al*. "A Study of Build Edge Profile for Prediction of Surface Roughness in Fused Deposition Modeling". *Journal of Manufacturing Science and Engineering*. Vol. 138, No. 6, pages 061002–061002–11. 2016.

[11] Alsoufi *et al*. "How Surface Roughness Performance of Printed Parts Manufactured by Desktop FDM 3D Printer with PLA+ is Influenced by Measuring Direction". *American Journal of Mechanical Engineering*. Vol. 5, No. 5, pages 211–222. 2017.

[12] Briscoe *et al*. "Wear of polymers". *Proceedings of the Institution of Mechanical Engineers, Part J: Journal of Engineering Tribology*. Vol. 216, No. 6, pages 401–413. 2002.

[13] Myshkin *et al*. "Tribology of polymers: Adhesion, friction, wear, and mass-transfer". *Tribology International*. Vol. 38, No. 11, pages 910–921. 2005.

[14] Rymuza. "Tribology of Polymers". *Archives of Civil and Mechanical Engineering*. Vol. 7, No. 4, pages 177–184. 2007.

[15] Unal *et al*. "Friction and wear performance of polyamide 6 and graphite and wax polyamide 6 composites under dry sliding conditions". *Wear*. Vol. 289, pages 132–137. 2012.

[16] ASTM-D1984-14. *Standard Test Method for Static and Kinetic Coefficients of Friction of Plastic Film and Sheeting*. Standard. West Conshohocken, PA: ASTM International, 2014.

[17] "Volume 18: Friction, Lubrication, and Wear Technology". In: edited by Totten. ASM Handbook. Washington, DC, 2017.

[18] Ellis *et al*. Editors. *Polymers: a property database*. Second. CRC Press, 2008.

[19] Bashford, editor. *Thermoplastics: directory and databook*. First. Chapman & Hall, 1996.

[20] Difallah *et al*. "Mechanical and tribological response of ABS polymer matrix filled with graphite powder". *Materials & Design*. Vol. 34, pages 782–787. 2012.

[21] Leacock *et al*. "Structural and Frictional Performance of Fused Deposition Modelled Acrylonitrile Butadiene Styrene (P430) with a view to use as Rapid Tooling Material in Sheet Metal Forming." *Key Engineering Materials*. Vol. 639, pages 325–332. 2014.

[22] Gurrala *et al*. "Friction and wear behavior of abs polymer parts made by fused deposition modeling (FDM)". In: *International Conference on Advances of Tribology*. 2014.

[23] Dawoud *et al*. "Effect of processing parameters and graphite content on the tribological behaviour of 3D printed acrylonitrile butadiene styrene". *Materialwissenschaft und Werkstofftechnik*. Vol. 46, No. 12, pages 1185–1195. 2015.

[24] Boparai *et al*. "Wear behavior of FDM parts fabricated by composite material feed stock filament". *Rapid Prototyping Journal*. Vol. 22, No. 2, pages 350–357. 2016.

[25] Perepelkina *et al*. "Investigation of friction coefficient of various polymers used in rapid prototyping technologies with different settings of 3D printing". *Tribology in Industry*. Vol. 39, No. 4, page 519. 2017.

[26] Beg *et al*. "Investigation on tribological behavior of FDM printed ABS polymer". *International Journal of Technical Research and Applications*. Vol. 5, pages 75–77. 2017.

[27] Farstad *et al*. "Surface Friction of Rapidly Prototyped Wheels from 3D-Printed Thermoplastic Elastomers: An Experimental Study". *Procedia CIRP*. Vol. 60, pages 247–252. 2017.

[28] Sood *et al*. "Parametric appraisal of fused deposition modelling process using the grey Taguchi method". *Proceedings of the Institution of Mechanical Engineers, Part B: Journal of Engineering Manufacture*. Vol. 224, No. 1, pages 135–145. 2010.

[29] Equbal *et al*. "Prediction and analysis of sliding wear performance of fused deposition modelling-processed ABS plastic parts". *Proceedings of the Institution of Mechanical Engineers, Part J: Journal of Engineering Tribology*. Vol. 224, No. 12, pages 1261–1271. 2010.

[30] Sood *et al*. "An investigation on sliding wear of FDM built parts". *CIRP Journal of Manufacturing Science and Technology*. Vol. 5, No. 1, pages 48–54. 2012.

[31] Bowden *et al*. "The ploughing and adhesion of sliding metals". *Journal of Applied Physics*. Vol. 14, No. 2, pages 80–91. 1943.

[32] *ABSPlus-P430 for Fortus 3D Production Systems*. STRATASYS.

[33] ASTM-D732-17. *Standard Test Method for Shear Strength of Plastics by Punch Tool*. Standard. West Conshohocken, PA: ASTM International, 2017.

[34] Bowden *et al*. *The Friction and Lubrication of Solids*. Oxford, 1954.

[35] Yamaguchi. *Tribology of plastic materials: their characteristics and applications to sliding components*. Volume 16. Elsevier, 1990.

[36] Tabor. "Friction, Adhesion and Boundary Lubrication of Polymers". In: *Advances in Polymer Friction and Wear*. Edited by Lee. Boston, MA: Springer US, 1974, pages 5–30.

[37] Blau. *Friction Science And Technology From Concepts to Applications*. CRC press, 2008.

[38] Van Beek. *Advanced engineering design: lifetime performance and reliability*. Delft : TU Delft, 2009.

[39] Greenwood *et al*. "Contact of nominally flat surfaces". *Proceedings of the Royal Society of London. Series A. Mathematical and Physical Sciences*. Vol. 295, No. 1442, pages 300–319. 1966.

[40] Radzimovsky. *Stress distribution and strength condition of two rolling cylinders pressed together*. Technical report. University of Illinois at Urbana Champaign, College of Engineering. Engineering Experiment Station., 1953.

[41] Young *et al*. *Roark's formulas for stress and strain*. Volume 7. McGraw-Hill New York, 2002.

[42] Pereira *et al*. "A critical overview of internal and external cylinder contact force models". *Nonlinear Dynamics*. Vol. 63, No. 4, pages 681–697. 2011.

[43] Skrinjar *et al*. "A review of continuous contact-force models in multibody dynamics". *International Journal of Mechanical Sciences*. Vol. 145, pages 171–187. 2018.

[44] Johnson. *Contact Mechanics*. Cambridge University Press, 1985.

[45] Flores *et al*. *Contact force models for multibody dynamics*. Volume 226. Springer, 2016.

[46] Puttock *et al*. *Elastic compression of spheres and cylinders at point and line contact*. Commonwealth Scientific and Industrial Research Organization Melbourne, Australia, 1969.

[47] Williams *et al*. "Contact between solid surfaces". *Modern tribology handbook*. Vol. 1, pages 121–162. 2001.

[48] Amuzu *et al*. "Friction and Shear Strength of Polymers". *A S L E Transactions*. Vol. 20, No. 4, pages 354–358. 1977.

[49] Armstrong-Helouvry. *Control of machines with friction*. Volume 128. Springer Science & Business Media, 2012.

[50] Armstrong-Helouvry. "Stick-slip arising from Stribeck friction". In: *Proceedings., IEEE International Conference on Robotics and Automation*. Vol. 2, pages 1377–1382. 1990.

[51] Hess *et al*. "Friction at a Lubricated Line Contact Operating at Oscillating Sliding Velocities". *Journal of Tribology*. Vol. 112, No. 1, pages 147–152. 1990.

[52] Bo *et al*. "The friction-speed relation and its influence on the critical velocity of stick-slip motion". *Wear*. Vol. 82, No. 3, pages 277–289. 1982.

[53] Al-Bender *et al*. "Modeling of dry sliding friction dynamics: From heuristic models to physically motivated models and back". *Chaos: An Interdisciplinary Journal of Nonlinear Science*. Vol. 14, No. 2, pages 446–460. 2004.

[54] B.Sc. "CVI. A molecular theory of friction". *The London, Edinburgh, and Dublin Philosophical Magazine and Journal of Science*. Vol. 7, No. 46, pages 905–939. 1929.

[55] Kato *et al*. "Some Considerations on Characteristics of Static Friction of Machine Tool Slideway". *Journal of Lubrication Technology*. Vol. 94, No. 3, pages 234–247. 1972.

[56] Rabinowicz. *Friction and Wear of Materials, Jhon Wiley & Sons*. 1995.

[57] *GitHub repository for experimental measurements and analytical codes*. http://bit.ly/2SloTYc.

[58] Schneider *et al*. "Laser Textured Surfaces for Mixed Lubrication: Influence of Aspect Ratio, Textured Area and Dimple Arrangement". *Lubricants*. Vol. 5, No. 3, 2017.

[59] Schneider *et al*. "Friction reduction through biologically inspired scale-like laser surface textures". *Beilstein Journal of Nanotechnology*. Vol. 9, No. 1, pages 2561–2572. 2018.

4. Introducing PneuAct-II

Note: The following content is an adapted version of the paper "PneuAct-II: Hybrid Manufactured Electromagnetically Stealth Pneumatic Stepper Actuator" by F. Sojoodi Farimani, M. Mojarradi, E. Hekman, and S. Misra, IEEE Robotics and Automation Letters (RA-L), volume 5, issue number 2, pages 3588–3593, April 2020. ■

Abstract

Additive Manufacturing (AM) is one of the emerging production methodologies transforming the industrial landscape. However, application of the technology in fluidic power transmission and actuation is still limited. AM Pneumatic Stepper Motors (PSMs) have been previously introduced to the field of image-guided surgical robotics, where their disposability and customizability are considered a significant advantage over conventional manufacturing. However, intrinsic dimensional limitations of AM parts and their poor surface quality affect mechanical performance. In this study, a novel design, PneuAct-II, is presented combining AM, subtractive machining, and off-the-shelf components to achieve higher mechanical performance and resolution. Moreover, a motor characterization setup has been built to automatically measure different aspects of the PneuAct motors, including wear, friction, leakage, and stall behavior at various boundary conditions. The effects of input pressure, stepping frequency, signal width, and external torque on the stall behavior of motors with different clearances are studied. A maximum torque of $0.39\,\mathrm{N\cdot m}$ at an input pressure of $6.5\,\mathrm{bar}$ is achieved for a motor with a total volume of $90\,\mathrm{cm^3}$, and a clearance of $156\,\mu\mathrm{m}$. A nominal resolution of 2.25° at full-pitch and 1.125° at half-pitch is accomplished. Both resolution and mechanical performance ($667\,\mathrm{N\cdot m/bar/m^3}$) outperform the state-of-the-art ($240\,\mathrm{N\cdot m/bar/m^3}$ by PneuAct-I).

The PneuAct-II design surpasses its predecessor by blending additive manufacturing with subtractive techniques and standard parts, improving mechanical performance and resolution significantly. This approach not only sets new standards in the domain but also demonstrates the potential of hybrid manufacturing methods in overcoming additive manufacturing challenges, especially in precise engineering applications like image-guided surgical robotics.

4.1 Introduction

Different industries prefer fluidic actuators (i.e., hydraulic and pneumatic) over conventional Electromagnetic (EM) motors due to their high mechanical output-to-size ratio, resilience towards harsh environments, and safety [1]. For instance, being intrinsically non-electromagnetic, they do not require extensive shielding in explosive atmospheres. They can easily survive environments with high ionizing radiation (e.g., nuclear power plants), high humidity, and corrosive substances. Given the right materials and components (i.e., nonconductive and low magnetic susceptibility), fluidic actuators can be electromagnetically stealth. They can be used in sensitive environments such as the vicinity of Magnetic Resonance (MR) imaging machines. In particular, pneumatic actuators have several advantages over hydraulics in image-guided minimally invasive interventions because high pressurized air is abundantly available in hospitals, and possible leakages do not interfere with MR imaging nor hinder the safety of the operation [2].

Pneumatic actuators were introduced to the Magnetic Resonance Imaging (MRI)-guided robotic-assisted minimally invasive surgery field by Hempel *et al.* (2003) [3] in the form of conventional linear cylinder-pistons. One major issue with conventional pneumatic actuators is their unpredictable behavior, making position control challenging [4]. Air, being a compressible and viscous fluid, can behave chaotically when used as a power transmission medium, leading to uncontrollable overshoots if used in a robotic system [5]. Elhawary *et al.* (2007) [6], Tse *et al.* (2008) [7], and Chen *et al.* (2017) [8] also presented rotational pneumatic motors using turbine or vane mechanisms. Continuous fluidic actuators, volumetric or dynamic, offer higher speeds than stepper motors. However, implementing a reliable and accurate position control with continuous pneumatic actuators in the MR environment is difficult. Considering these limitations, several groups have been developing rotational fluidic stepper motors, such as the one developed in this study (figure 4.1). Being limited-state machines, stepper actuators have a more straightforward and reliable motion control than servo actuators, even without position feedback (i.e., open-loop control).

The first mentions of fluidic stepper motors can be traced back to a patent by Musser (1963) [9] in the mid-nineteen-hundreds, inspired by his other invention, Harmonic Drive®. Suzumori *et al.* (1998) [10]

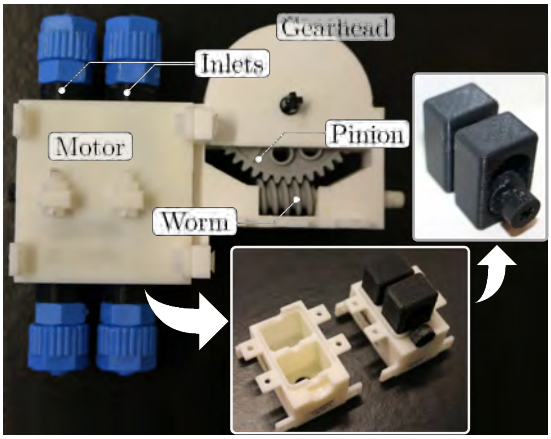

Figure 4.1: A PneuAct-II actuation set including the motor and worm-pinion reduction drive (figure 4.3). Two double-sided pistons, assembly-printed with the crankshaft, generate reciprocating motions following the pneumatic excitation patterns moderated by the Electro-Pneumatic Control Unit (EPCU) (figure 4.2). The linear motion is consequently converted to rotation through the Scotch Yoke mechanism. The gear-head comprises a 3D printed body encompassing standard off-the-shelf LEGO® parts, together forming a slewing reduction drive of 40:1 ratio.

were the first group to implement a rotational PSM in the last decade of the 20th century. However, the presented prototypes were not MR-compatible. Taillant *et al*. (2004) [11] demonstrated the first rotational MR-compatible PSM for the Light Puncture Robot (LPR). Stoianovici *et al*. (2007) [12] reported a significant implementation of the concept, PneuStep actuator, used in the minimally invasive prostate intervention mechanism, MrBot. Nonetheless, affordability and disposability required for a surgical setting have not been considered. Slightam *et al*. (2012) [13] and Wei *et al*. (2016) [14] utilized AM and non-assembly printing to develop pneumatic actuation in the form of a flexible chamber or turbine. However, the presented prototypes are not stepper actuators, requiring position feedback.

PneuAct-I was introduced as a fully 3D-assembly-printed pneumatic stepper actuator for the position control of robotic mechanisms in environments where EM motors are not permitted [15]. PneuAct-I aimed to be a paradigm shift in the field by providing a parametrically de-

signed, affordable, disposable, recyclable, high resolution, safe (in terms of delivering passive backdrivability), high speed, and electromagnetically stealth rotational pneumatic stepper actuator. Similarly, Boland *et al*. (2019) [16] presented a fully AM rotational PSM, with a maximum torque of $0.19\,\mathrm{N\cdot m}$ and a speed of 2000 RPM at 6.2 bar input pressure, in a total volume of $512\,\mathrm{cm}^3$. Their prototype delivered a mechanical performance of $60\,\mathrm{N\cdot m/bar/m}^3$ and a raw resolution of 90°. In comparison, PneuAct-I delivered a mechanical performance of approximately $240\,\mathrm{N\cdot m/bar/m}^3$ (4 times higher) with a maximum holding torque of $0.14\,\mathrm{N\cdot m}$, a resolution of 3° at an input pressure of 6.5 bar and an approximate total volume of $90\,\mathrm{cm}^3$.

However, more efficient actuators in the same form factor and price range could significantly improve the usability and application value. PneuAct-II is a significant redesign of the rotational PSMs towards improving mechanical performance and resolution while sustaining the production costs and minimal size. To that end, a hybrid manufacturing methodology, Computer Numerical Control (CNC) milling of the 3D-printed parts, is adopted to improve the surface quality of the AM parts in critical areas where friction and leakage are problematic. Injection-molded off-the-shelf LEGO® parts have been incorporated in the gearbox to deliver better performance while keeping costs minimal. Using Commercially available Off-The-Shelf (COTS) significantly improved performance while lowering production time and cost. Affordability is a major factor when designing a disposable surgical accessory.

A motor characterization setup is presented for the first time in the field, which can isolate and characterize different aspects of the PSMs, including internal friction, leakage, and stall behavior under various design and boundary conditions. The combination of hybrid manufactured PSM, PneuAct-II, and the gear-head reduction drive with COTS LEGO parts can sustain a maximum stall torque of $0.39\,\mathrm{N\cdot m}$ at an input pressure of 6.5 bar, delivering 2.7 times better mechanical performance than the previous version. A resolution of 2.25° at the full-pitch drive and 1.125° at the half-pitch is delivered, improving the latest records in the field.

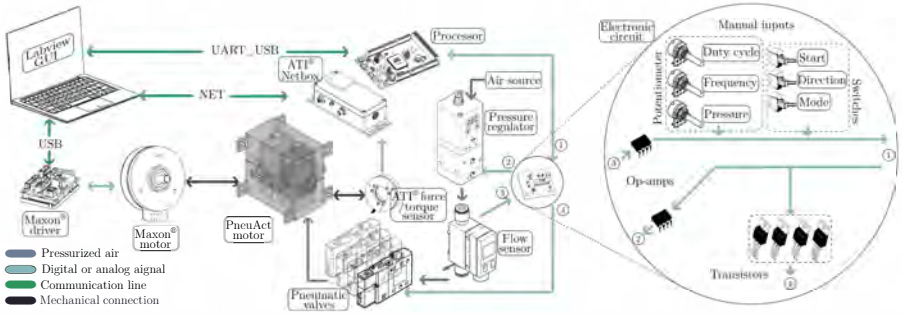

Figure 4.2: A schematic diagram of the Electro-Pneumatic Control Unit (EPCU) and the motor characterization setup: The Electro-Pneumatic Control Unit (EPCU) generates the square wave excitation signals to control the pneumatic valves. It also controls the pressure regulator while reading the airflow rates from the flow meter. Different parameters, including the input pressure, duty cycle, and stepping frequency, can be controlled directly from the LabVIEW® Graphical User Interface (GUI) or manually from the boards using the potentiometers and switches. The motor characterization setup includes the Maxon® EC motor, which sends and receives data from the computer through the driver, and the Nano43® sensor sends six values (three forces and three torques) to the computer through the Netbox.

4.2 Materials and Methods

Every PneuAct-II actuation set contains two main sections: the mechanical modules, including the gear-head and motor, and the Electro-Pneumatic Control Unit (EPCU). In the following paragraphs, these sections, their submodules, relationships and functionalities are described:

4.2.1 Mechanical Design

The mechanical section of the PneuAct-II actuator consists of two modules, the motor itself and the gear-head:

Motor

PneuAct-II employs a Scotch Yoke mechanism (also known as the slotted link mechanism) to convert the reciprocating motion of the pistons to rotation (figure 4.3). The mechanism is kinematically analogous to PneuAct-I, except in the new version, the two double-acting cylinders-pistons offer four steps-per-revolution instead of three one-sided pistons [15]. PneuAct-II has a better raw resolution than the previous generation as it has a step-size of 90° at full-pitch instead of 120° previously reported and a half-pitch step-size of 45° instead of 60°.

The motor comprises four parts printed in three components, including the two identical segments of the cylinder-heads, and the assembly-printed combination of the crank-shaft plus two pistons (figure 4.3). The crank-shaft has two off-centric crank-pins with a 90° degrees phase-shift, which slide in the slotted body of the pistons. Pistons are actuated through the excitation pressure signal (i.e., square wave signal) generated by the EPCU. The parts are 3D printed with a Stratasys® (Rehovot, Israel) Fortus-250mc® machine using ABSplus™-P430 material with a nominal layer thickness of 0.1778 mm[1]. To improve energy efficiency and reduce leakage and friction, cylinder heads are machined with different clearances (100-250) µm. PneuAct-II is designed with modularity in mind. The standard plus-shaped (+) LEGO® (Billund, Denmark) connector is placed at both sides of the motor and the gearhead. It means several motors can be put in series to improve resolution and torque. The connection can also be used to mount the gearhead, position encoder, torque sensor, and clutch/brake.

[1]This is the minimum layer heights that can be achieved with 3d printer

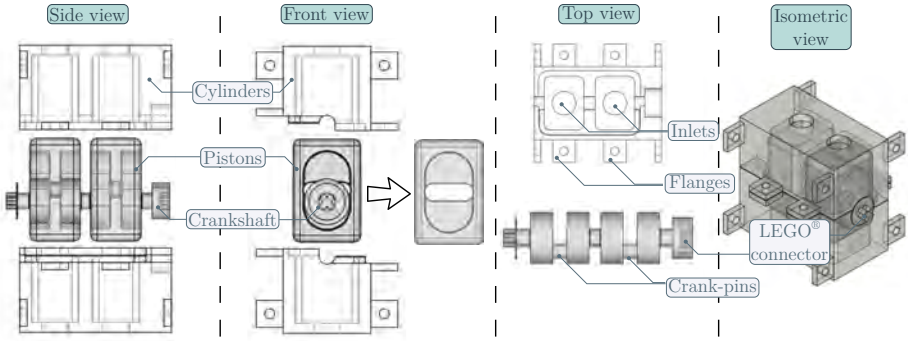

Figure 4.3: Exploded and isometric views of the PneuAct-II motor designed in Free, Libre, and Open Source Software (FLOSS) Computer Aided Design (CAD) software FreeCAD. The motor comprises three parts printed separately, including the two identical cylinder heads and the assembly-printed combination of two pistons and the crankshaft. The shaft includes male and female standard plus-shaped (+) LEGO® connectors on both ends to account for the modularity of the design. The two double-sided pistons constitute four chambers working like a four-piston engine, and the Scotch Yoke mechanism converts reciprocating motion to torque.

Gear-head

In PneuAct-I, the entire gearhead was 3D-printed to achieve high affordability and customizability. However, for non-assembly-printing with a Fortus-250mc® printer, a small gap of 0.3 mm needs to be included between adjacent surfaces, to avoid interfusion. Not only can the gap introduce some backlash, but it may also result in some actuation steps being skipped at high external torques — this affects both the mechanical performance and the actuator's accuracy. Furthermore, the Fused Deposition Modeling® (FDM)® manufactured parts suffer from an inferior surface quality (in comparison to other AM methods). As a result, the fully FDM-manufactured assembly-printed gear-head delivered a low energy efficiency and poor determinism.[2]

In PneuAct-II, the gearhead comprises a 3D-printed body encompassing off-the-shelf injection molded parts with better dimensional accuracy and surface quality. A worm-pinion reduction drive of 40:1 gear-ratio (similar to the one used for PneuAct-I) has been developed, except

[2]It is conceivable that other 3D printing technologies such as Formlabs Stereolithography (SLA) might be able to alleviate these issues

here LEGO® gear-pinion (part numbers 3649 and 4716) have been used to improve energy efficiency and alleviate backlash/play. The use of precision-manufactured LEGO® components not only ensures consistent mesh engagement between the worm and pinion gears but also provides reliable long-term operation due to their wear-resistant material properties. The combination of 3D-printed housing and commercial gear components results in a hybrid design that balances cost-effectiveness with mechanical reliability. A nominal final resolution of 2.25° at full-pitch and 1.125° at half-pitched is achieved, which are improvements over 3° and 1.5° of PneuAct-I.

4.2.2 Electro-Pneumatic Control Unit (EPCU)

EPCU generates the square wave signal, controlling solenoid pneumatic valves, given the duty-cycle (or signal width) and stepping frequency. The amplitude of the pneumatic waves is modulated via a Festo® (Esslingen, Germany) VPEE pressure regulator ($(2\text{-}7.5)$ bar). Rotational direction (i.e., clockwise or counterclockwise) and control mode (position and speed) can be selected using on-board switches. The EPCU also reads the flow from a Festo® SFAB sensor. The above parameters can be controlled via physical knobs (potentiometers) and switches on the electronic board or via the LabVIEW® (National Instruments™: Austin, United States) graphical user interface on the computer, through serial communication.

The EPCU's design prioritizes flexibility and ease of integration, allowing for both manual control during experimental setup and automated operation during systematic testing. This dual-control capability is particularly valuable for characterizing the motor's performance across different operating conditions. The system's ability to precisely regulate pressure and timing parameters, while simultaneously monitoring airflow, enables comprehensive analysis of the pneumatic actuator's behavior. Furthermore, the modular nature of the control system allows for future expansions and modifications, such as the integration of additional sensors or the implementation of more sophisticated control algorithms, making it a versatile platform for both research and potential clinical applications.

4.2.3 Motor characterization Setup

In previous studies, two different methods were used to measure the output torque of the motors. The first method is to use a cable and pulley coupled rotationally to the output shaft of the motors to lift some weights or deform a compliant energy storage component (i.e., spring). Another approach is to use dynamometers, which measure the instantaneous exerted power of the motors. In this study, a motor characterization setup has been made to measure different aspects of the PneuAct-II motor (figure 4.4). The setup comprises a Maxon® (Friedrichsdorf, Germany) EC motor, an ATI® (NC, USA) 6-Degree of Freedom (DOF) force/torque (F/T) sensor, and a laser-cut mechanical structure encompassing the PneuAct-II motor. The Maxon® motor can be torque or velocity-controlled at different phases of the experiments while data is being collected from the F/T sensor, EM motor's driver, and EPCU.

The integration of these precise measurement instruments allows for comprehensive characterization of motor behavior under various operating conditions. While traditional methods primarily focus on measuring output torque, this setup enables simultaneous monitoring of multiple parameters including friction, stall conditions, and dynamic response. The ability to switch between torque and velocity control modes of the Maxon® motor, combined with the high-precision measurements from the ATI® F/T sensor, provides detailed insights into the motor's performance characteristics. This level of detailed analysis is particularly crucial for understanding the behavior of pneumatic actuators in medical applications, where precise control and reliable performance are paramount.

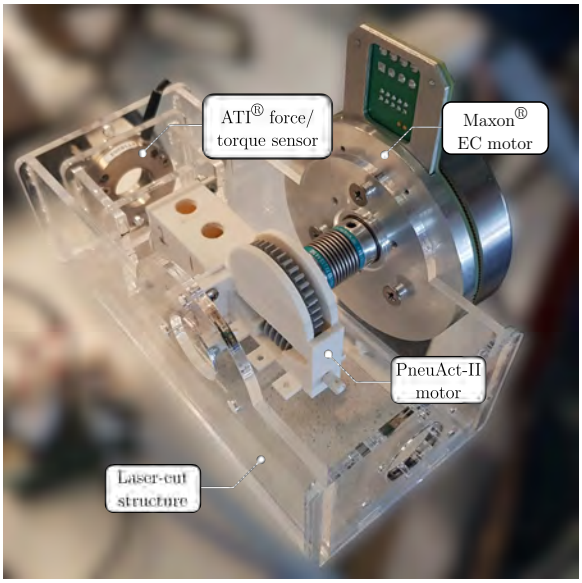

Figure 4.4: The motor characterization setup comprises a 6-Degree of Freedom (DOF) force/torque sensor, a Maxon® EC motor with torque and speed control. The laser-cut structure encompasses the PneuAct-II motor and the gearhead. The Maxon® motor can be mounted to the motor's shaft or the gear-box output for different phases of the experiments.

4.3 Experiments and Results

Several experiments are designed to isolate and characterize different properties of the PneuAct-II motors, identifying the stall points at various boundary conditions. Initially, the freshly 3D-printed motor and the gear-head are placed in the experimental setup, and the Maxon® motor rotates them through the worm-gear shaft at a constant speed. The required torque is recorded through both the EM motor's encoder and the F/T sensor. Torque changes over time, representing wear in the motor and gearhead. This experiment is continued until the torque asymptotes to a constant value, indicating that wear has stabilized.

Consequently, to identify the stall behavior of the PneuAct motors, they are actuated at different speeds (i.e., stepping frequencies), duty cycles, and input pressures. At the same time, the external torque is applied up to a maximum of $0.5\,\mathrm{N}\cdot\mathrm{m}$ (figure 4.9). The position of the motors is recorded throughout the experiments. The experiments are repeated

for different boundary conditions: stepping frequencies ((1-25) Hz), duty-cycles ((25, 50, 75 and 100) %), and input pressures ((2-7.5) bar). Experiments are conducted on machined motors with different clearances ((120-270) µm). Figures 4.5 to 4.8 show the bootstrapped results of the above experiments for a PneuAct-II motor with a piston dimension of 15×20 mm, and a stroke length of 8 mm. [3]

Figure 4.5 shows the average behavior of the stall torque at different input pressures. The minimum required pressure for actuating the motor is approximately 3 bar to overcome internal friction in the system. The overall relationship is proportional, which is in agreement with the simplified energy equilibrium equation describing the average dynamic behavior of the system:

$$\tilde{\tau}\tilde{\omega} < \tilde{P}\tilde{Q}, \tag{4.1}$$

where

$\tilde{P}$ = Average input pressure (bar)
$\tilde{\tau}$ = Average external torque ($\mathrm{N} \cdot \mathrm{m}$)
$\tilde{\omega}$ = Average angular speed (rad/s)

and $\tilde{Q}$ is the average air flow in (m^3/s) calculated as:

$$\tilde{Q} = V_0 n \frac{\tilde{\omega}}{2\pi}, \tag{4.2}$$

and

V_0 = is the maximum volume of the chamber (m^3)
n = number of cylinders (4 for PneuAct-II)

Substituting $\tilde{Q}$ from equation (4.2) in equation (4.1) and omitting $\tilde{\omega}$ from both sides shows that the stall behavior should be independent of speed or stepping frequency ($f_s = n\omega/2\pi$).

[3] experimental data and analysis code can be acquired at GitHub repository [17]

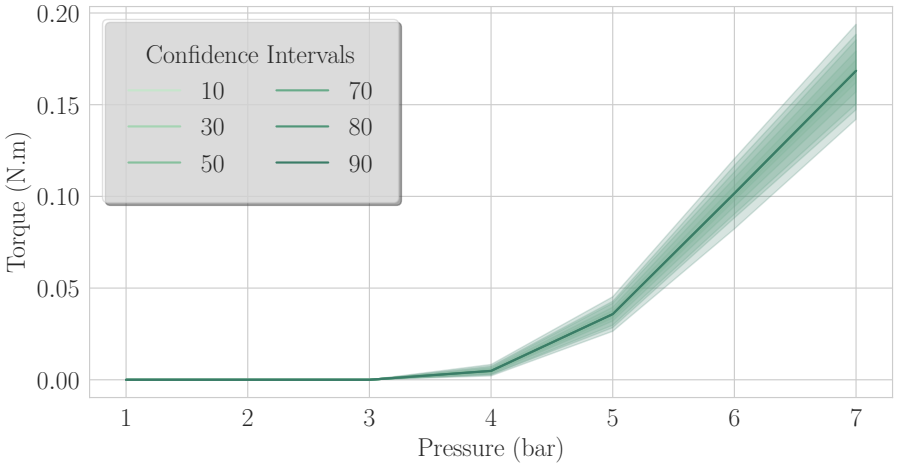

Figure 4.5: Bootstrapped stall torque is plotted at various input pressures contoured with different confidence intervals. A linear relationship can be observed as predicted by equation (4.1) while an average minimum pressure of 3 bar is required to overcome internal friction and leakage.

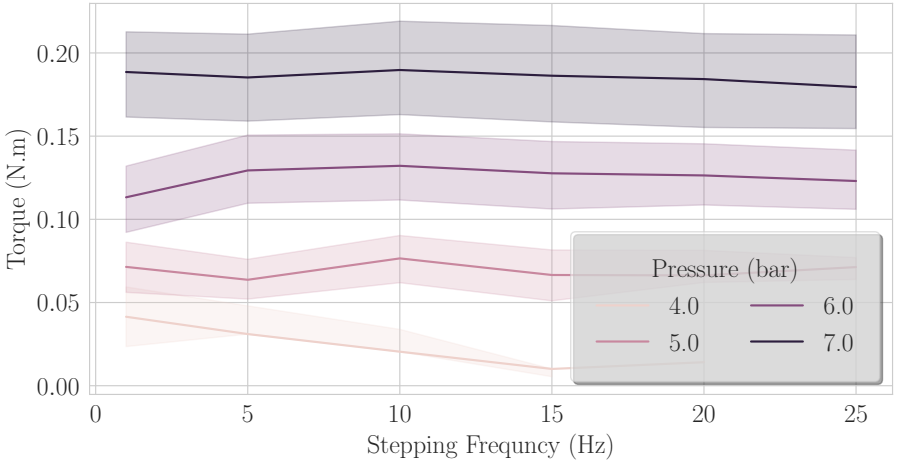

Figure 4.6: Stall torque versus stepping frequency is plotted at various input pressures with a confidence interval of 50 %. No significant relationship between torque and stepping frequency (i.e., rotational speed) is observed.

Figure 4.6 illustrates the overall relationship between the stall torque and stepping frequency at different input pressures. The significance of the graph is in demonstrating the above prediction that the stall torque does not theoretically depend on the motor's rotational speed. This contradicts previous studies, where a negative relationship between stall torque and rotational speed was reported. As equations (4.1) and (4.2) shows, if the effects of speed on leakage and friction are neglected, the stall torque should be independent of the motor's frequency. Previous studies, including the study done by the authors [15], have identified a negative relationship between stall torque and stepping frequency because a constant duty cycle has been maintained throughout the experiments. Hence, higher frequencies lead to smaller signal width, and less energy is pumped to the motors.

The solenoid valves have a rise-time and minimum pilot pressure, which is required to overcome their internal static friction. Also, propagation of the pressure signals through the tubing causes delay and dissipation, as presented in the previous study [15]. As a result, signal widths and pressures below certain thresholds lead to unstable behavior of the valves. This can be seen in figure 4.7 where signal widths below 9 ms result in somewhat unstable behavior.

Figure 4.8 shows the stall torque of the motors with different clearances at various input pressures. This graph represents the trade-off between friction and leakage in PneuAct-II actuators. At smaller gap sizes, the normal force between two sliding surfaces increases friction while increasing the clearance would raise leakage. As a result, there is an optimum clearance where the energy efficiency of the PneuAct motor is at its maximum. The optimum clearance, as measured in the experiments, is approximately 150 µm, which is in agreement with the value reported in the previous study by the authors for fully 3D-printed motors [15].

One significant observation in this study was the inverse motion of the motors in certain conditions. The worm-pinion reduction-derives are usually self-locking; hence, the external torque on the pinion's shaft should not be able to rotate the gearbox in the opposite direction. However, during the experiments, a negative rotation in the PneuAct motor was observed (figure 4.9). Further investigation revealed that this behavior can be attributed to the stall phenomenon. Basically, when the PneuAct

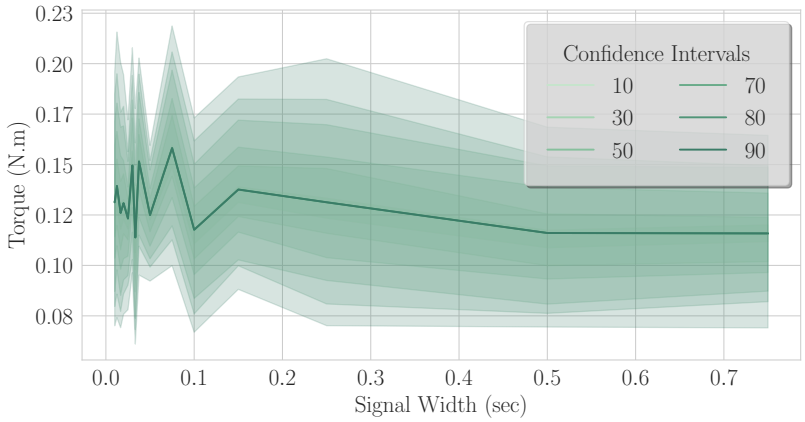

Figure 4.7: The stall torque is plotted against signal width, contoured at different confidence intervals. The plot demonstrates that the stall behavior is independent of the signal width while it is above a certain threshold. The PneuAct motor behaves chaotically when signal widths are below the threshold due to the valve's rise time and their minimum pilot pressure.

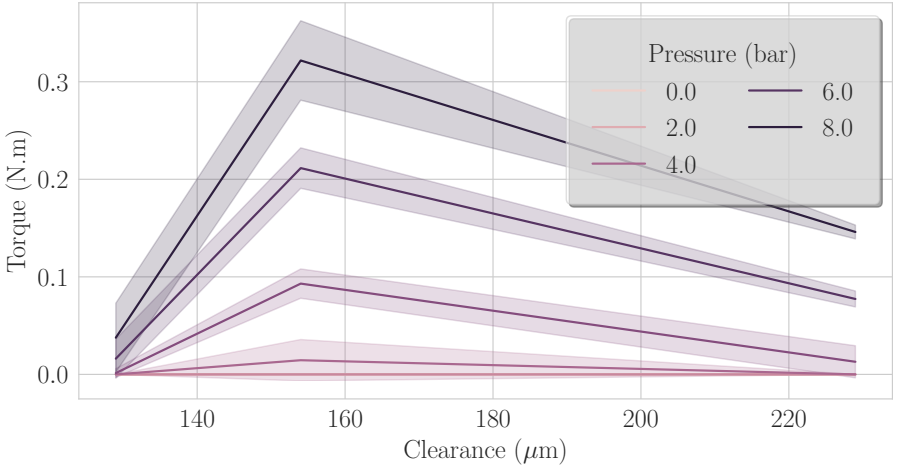

Figure 4.8: The stall torque is plotted for motors with various clearances (i.e., average gap size between the pistons' perimeter and the cylinders) at different input pressures. The error band's width is the standard deviation. The plot demonstrates the interaction between leakage and friction at different clearances, showing optimum performance at 150 µm.

motor experiences a stall, some steps are skipped. As a result, while the crank pin is in the wrong position, the following steps can rotate the motor in the opposite direction where there is no opposing potential.

It was previously presumed that PSMs, in contrast to continuous actuators, can deliver relatively precise position control in an open-loop configuration. This was considered an advantage over servo actuators such as turbines and vane motors. Considering that common position encoders and their circuitry are usually not MR compatible and that it is generally difficult to make EM stealth sensors of any kind. However, this observation implies that even stepper motors require a position encoder if safe and reliable position control, which is highly required in a surgical application, is to be expected.

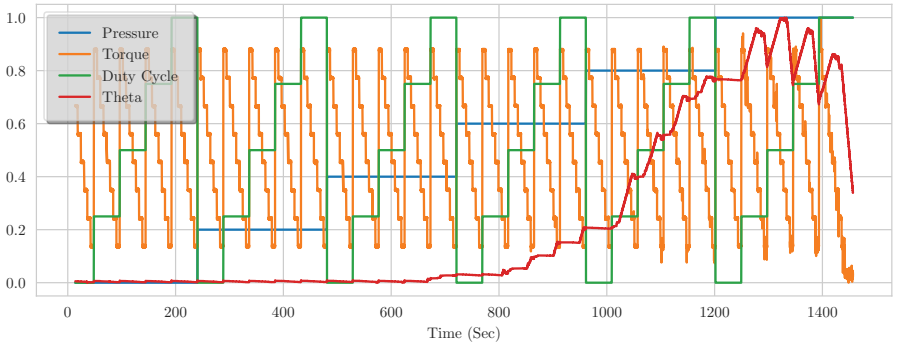

Figure 4.9: The stall behavior of a PneuAct-II in Step 1. of Phase3., in a sample with a clearance of 224 µm at various input pressures, external torques, and duty-cycles is illustrated in a normalized plot. Constant Theta (i.e., position) represents the stall of the PneuAct actuator. In certain conditions, especially at high pressures, the PneuAct motor rotates in the opposite direction (i.e., reducing Theta) due to the missing-steps phenomenon, as the text explains.

4.4 Conclusions

This study introduces a significant redesign of 3D-printed and parametrically designed PSMs. A hybrid manufacturing approach is employed where the cylinders are machined to alleviate leakage and friction. A new mechanical design with two double-acting cylinder pistons is presented to improve machinability, resolution, and backlash. In comparison to PneuAct-I, the new version generates 2.7 times higher mechanical per-

formance while keeping the production time/costs minimal. The new version has a better resolution of 2.25° at full-pitch, breaking the previous record in the field by PneuAct-I, and a resolution of 1.125° at half-pitch. It was shown that there is no significant relation between stall torque and stepping frequency as long as the signal width is above a certain threshold determined by the rise time of the solenoid valves and the dimension (length and diameter) of the pneumatic tubes. Although this is in contrast to the previous studies, it is in agreement with the more accurate mathematical model.

A motor characterization setup, comprising a 6-DOF force/torque sensor and an EM stepper motor with speed and torque control, is developed to measure different aspects of the PneuAct-II motor. The setup can measure internal friction, pneumatic efficiency, minimum required signal width at specific input pressure and external torque, and stall torque at specific input pressure and stepping frequency. This allowed measuring aspects of the PSM, which was impossible with conventional methods. This study also demonstrated that backdrivable PSMs might not deliver reliable position control in an open-loop configuration, concluding that encoders are necessary for safety. A follow-up work for this project could be to develop such an encoder based on a similar design rationale and manufacturing principles.

In this study, a groundbreaking enhancement was achieved over the previous PneuAct-I design by incorporating a hybrid manufacturing process, which combined precision machining with 3D printing, to significantly reduce leakage and friction while enhancing resolution and mechanical performance. Our experiments revealed that contrary to prior assumptions, stall torque is not influenced by stepping frequency under certain conditions, challenging previous models and leading to a deeper understanding of the dynamics of PSMs. It was shown that through innovative design and a comprehensive experimental setup, it is possible to achieve superior performance in additive-manufactured PSMs, underscoring the importance of hybrid manufacturing techniques in advancing the field. This work not only sets a new benchmark in pneumatic actuator design but also lays a solid foundation for future advancements, highlighting the critical role of precision in enhancing the functionality and efficiency of 3D-printed mechanisms in robotics and beyond.

References

[1] Blackburn *et al*. *Fluid power control*. MIT Press, USA, 1960.

[2] Elhawary *et al*. "A Review of Magnetic Resonance Imaging Compatible Manipulators in Surgery". *Proceedings of the Institution of Mechanical Engineers, Part H: Journal of Engineering in Medicine*. Vol. 220, No. 3, pages 413–424. 2006.

[3] Hempel *et al*. "An MRI-Compatible Surgical Robot for Precise Radiological Interventions". *Computer Aided Surgery*. Vol. 8, No. 4, pages 180–191. 2003.

[4] Fischer *et al*. "MRI-Compatible Pneumatic Robot for Transperineal Prostate Needle Placement". *IEEE/ASME Transactions on Mechatronics*. Vol. 13, No. 3, pages 295–305. 2008.

[5] Comber *et al*. "Precision Position Tracking of MR-Compatible Pneumatic Piston-Cylinder Using Sliding Mode Control". In: *ASME 2011 Dynamic Systems and Control Conference and Bath/ASME Symposium on Fluid Power and Motion Control, Volume 1*. 2011.

[6] Elhawary *et al*. "A MR Compatible Mechatronic System to Facilitate Magic Angle Experiments in Vivo". In: *Medical Image Computing and Computer-Assisted Intervention – MICCAI 2007*. Pages 604–611. 2007.

[7] Tse *et al*. "A 3-DOF MR-Compatible Device for Magic Angle Related In Vivo Experiments". *IEEE/ASME Transactions on Mechatronics*. Vol. 13, No. 3, pages 316–324. 2008.

[8] Chen *et al*. "Robotic System for MRI-Guided Focal Laser Ablation in the Prostate". *IEEE/ASME Transactions on Mechatronics*. Vol. 22, No. 1, pages 107–114. 2017.

[9] Musser. "Fluid wave generator for harmonic drive". U.S. Patent 3088333. May 7, 1963.

[10] Suzumori *et al*. "A direct-drive pneumatic stepping motor for robots: designs for pipe-inspection microrobots and for human-care robots". In: *Proc. IEEE Int. Conf. on Robotics and Automation (ICRA)*. Vol. 4, pages 3047–3052. 1998.

[11] Taillant *et al*. "CT and MR Compatible Light Puncture Robot: Architectural Design and First Experiments". In: *Medical Image Computing and Computer-Assisted Intervention – MICCAI 2004: 7th International Conference, Saint-Malo, France, September 26-29, 2004. Proceedings,*

Part II. Edited by Barillot *et al*. Berlin, Heidelberg: Springer, 2004, pages 145–152.

[12] Stoianovici *et al*. "A New Type of Motor: Pneumatic Step Motor". *IEEE/ASME Transaction on Mechatronics*. Vol. 12, No. 1, pages 98–106. 2007.

[13] Slightam *et al*. "Novel integrated fluid-power actuators for functional end-use components and systems via selective laser sintering nylon". In: *23rd Ann Int Solid Freeform Fabrication Symp*. Pages 197–211. 2012.

[14] Wei *et al*. "Novel Design and 3D Printing of Nonassembly Controllable Pneumatic Robots". *IEEE/ASME Transactions on Mechatronics*. Vol. 21, No. 2, pages 649–659. 2016.

[15] Sojoodi Farimani *et al*. "Introducing PneuAct: Parametrically-Designed MRI-Compatible Pneumatic Stepper Actuator". In: *Proc. IEEE Int. Conf. on Robotics and Automation (ICRA)*. Pages 200–205. 2018.

[16] Boland *et al*. "High Speed Pneumatic Stepper Motor for MRI Applications". *Annals of Biomedical Engineering*. Vol. 47, No. 3, pages 826–835. 2019.

[17] *GitHub repository for experimental measurements and analytical codes*. http://bit.ly/2kr1rf3.

III Concluding Remarks

5. Conclusions

This chapter concludes my dissertation, revisiting the research questions and objectives that have guided my exploration of Magnetic Resonance (MR)-compatible pneumatic actuation for surgical robotics. The preceding chapters documented the journey of developing novel actuators, delving into the complexities of friction in additively manufactured components to achieve precision and reliability within the unique constraints of the Magnetic Resonance Imaging (MRI) environment. This concluding chapter synthesizes the key findings (table 5.1), highlighting the contributions made to the field and outlining a vision for the future of MRI-guided surgical robotics.

The following sections revisit the four core research questions addressed in this dissertation, summarizing the technical challenges, innovative solutions, and outcomes achieved through this research endeavor. Each section delves into specific aspects of the work, from actuator design and fabrication to tribological characterization, model-based control, and the broader implications for surgical robotics. This chapter aims to provide a concise and insightful summary of the knowledge gained,

the advancements made, and the potential impact of this research on the future of minimally invasive interventions.

Table 5.1: Comparative Analysis of Research Contributions

Aspect	**Previous Work**	**Our Contributions**
Actuator Design	Limited customizability	Fully parametric, rapidly manufacturable designs
Manufacturing	Traditional methods	Hybrid additive-subtractive techniques
Tribology	Generic models	Refined models for 3D-printed surfaces

5.1 Parametric mechanism Design

Addressing research question 1 , this dissertation focused on designing a pneumatic stepper actuator using rapid manufacturing techniques that offers customizable performance, affordability, disposability, backdrivability, and deterministic behavior for surgical robotic applications (table 5.2). This approach was crucial in overcoming one of the critical challenges in realizing the full potential of MRI-guided robotic surgery: developing actuators that can operate effectively within the constraints of the MRI environment.

As outlined in objective 1, the research explored a range of conceptual designs for pneumatic stepper actuators that could be readily fabricated using rapid manufacturing techniques such as 3D printing, desktop Computer Numerical Control (CNC) machining, and laser cutting. This focus

Table 5.2: Comparison of PneuAct Actuators with Existing MR-Compatible Actuators

Feature	Prior Art	PneuAct I	PneuAct II
MRI Compatibility	Limited (EM interference)	Fully Compatible	Fully Compatible
Manufacturability	Complex, costly, limited customizability	3D printed, cost-effective, customizable	Hybrid manufactured, enhanced performance, cost-effective, customizable
Resolution	Limited	3° (full-pitch)	2.25° (full-pitch)
Mechanical Performance (Nm/bar/m³)	Low	240	667
Backdrivability	Often not backdrivable	Backdrivable	Backdrivable
Disposability	Not disposable	Potentially disposable	Potentially disposable

Color Legend:
Yellow indicates improvement over prior art.
Green indicates significant improvement or innovation.

on rapid manufacturing, as detailed in chapter 2, ensured the actuators would be cost-effective, customizable, and potentially disposable, making them suitable for surgical environments where sterility is paramount.

The culmination of this research effort was the development of the PneuAct family of Pneumatic Stepper Motors (PSMs). These actuators, designed with modularity and customizability in mind, incorporate innovative mechanisms and design principles to achieve reliable and deterministic stepping motion, backdrivability, and overall system simplicity, addressing objective 3. As described in chapter 2, the actuators are constructed using MR-compatible materials, ensuring their safe and effective operation within the MRI environment without causing image artifacts or interference.

As specified in objective 2, a parametric design methodology was implemented, allowing the PneuAct motors to be easily tailored to meet specific surgical application requirements. As elaborated in chapter 4, actuator dimensions, such as cylinder diameter and stroke length, can be adjusted to achieve the desired torque output, while the number of cylinders and the gearbox can be modified to achieve the required step size and resolution. This customizability allows for the creation of actuators with specific performance characteristics optimized for various surgical tasks, such as needle biopsies, targeted drug delivery, and tissue ablation.

The development of the PneuAct actuator platform, documented in chapters 2 and 4 demonstrates the feasibility of using rapid manufacturing techniques to create high-performance, MR-compatible pneumatic actuators for surgical robotics. This research not only advances the field of electromagnetically stealth actuation but also highlights the potential of parametric design and 3D printing for creating customized and adaptable actuators for a wide range of medical and industrial applications, as noted in section 1.4.

5.2 Hybrid Manufacturing

Addressing research question 2, this dissertation explored how Additive Manufacturing (AM) and hybrid fabrication techniques can be effectively utilized to improve the performance, cost-effectiveness, and customizability of PSMs for surgical robots (table 5.3). AM, often referred to as

Table 5.3: Comparison of Manufacturing Techniques for MR-Compatible Actuators

Aspect	**Traditional Manufacturing**	**Pure Additive Manufacturing**	**Hybrid Manufacturing**
Precision	High	Moderate	High
Customizability	Low	High	High
Cost-effectiveness	Low for small batches	High for prototypes	Moderate
Production speed	Slow for small batches	Fast for prototypes	Moderate
Material options	Limited	Wide range	Wide range
Surface finish	Excellent	Good	Excellent

3D printing, has emerged as a transformative technology, revolutionizing the fabrication of complex and customized components. However, the inherent limitations of AM, particularly in achieving high surface quality and dimensional accuracy, can hinder its application in high-precision systems like surgical robots.

As outlined in objective 4, we explored and compared different AM technologies, focusing primarily on Fused Deposition Modeling® (FDM) for its accessibility and versatility. As documented in chapter 2, the initial PneuAct design utilized FDM to create complex geometries and enable rapid prototyping of actuator components.

A key aspect of this research involved investigating the use of hybrid manufacturing techniques, combining additive and subtractive methods to enhance surface quality, dimensional accuracy, and overall performance (objective 5). We explored the use of FDM in conjunction with CNC machining to improve the surface quality and dimensional accuracy of PneuAct PSMs. We investigated various machining parameters, including tool selection, feed rate, spindle speed, and depth of cut, to optimize the surface finish of 3D-printed components, particularly the PneuAct cylinders where friction and leakage are critical concerns. This hybrid manufacturing approach, combining the rapid prototyping capabilities of FDM with the precision of CNC machining, enabled us to create actuators with enhanced performance characteristics, including

reduced friction, minimized leakage, and improved overall efficiency.

To address the objective of developing a framework for optimizing the selection of AM and hybrid fabrication methods (objective 6), we created parametric G-code generation scripts using Python. These scripts automated the creation of CNC machine instructions based on the desired actuator dimensions and machining parameters, allowing for efficient and reproducible fabrication. This approach facilitated the exploration of different design iterations and the optimization of machining parameters, enhancing the overall development process.

Furthermore, we investigated the use of spectral analysis methods for real-time monitoring and optimization of the CNC machining process. By analyzing the frequency spectrum of vibrations generated during machining, we could accurately detect contact between the CNC mill and the workpiece, allowing for precise control of tool depth and feed rate. This approach enabled us to minimize vibrations, reduce tool wear, and improve surface quality, further enhancing the performance and reliability of the hybrid manufactured actuators.

The integration of additive and subtractive manufacturing techniques, as demonstrated in this research and highlighted in section 1.4, offers a promising pathway to overcome the limitations of purely AM and unlock the full potential of 3D printing for creating high-performance, customizable, and cost-effective pneumatic actuators for surgical robots. The research findings, particularly those presented in chapter 4, contribute to the growing body of knowledge in hybrid manufacturing, showcasing its potential for enhancing the design and fabrication of advanced mechatronic systems in various fields, including medical robotics.

5.3 Tribological Characterization

This dissertation addressed research question 3: How do surface characteristics and operating conditions influence friction and wear in 3D printed components, and how can this knowledge be used to refine friction models for improved design and control of mechatronic systems? This investigation was particularly crucial for developing pneumatic actuators for MRI-guided surgical robots, where precise control and reliable performance are paramount.

As outlined in objective 7, we conducted an investigation into the tribo-

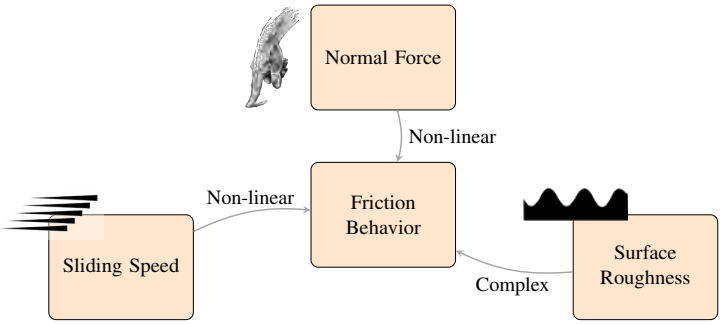

Figure 5.1: Summary of Key Tribology Findings for 3D-Printed Surfaces

logical properties of FDM-printed surfaces, characterizing their friction and wear behavior under a wide range of loading conditions, speeds, and surface configurations. As detailed in chapter 3, this research involved analyzing the influence of various factors, including normal force, sliding speed, surface roughness, contact area, and the relative alignment of printed layers. We employed a specialized test apparatus to accurately measure frictional forces, enabling us to isolate the effects of different parameters and obtain reliable data for model development and validation.

As specified in objective 8, we investigated the effects of AM process parameters on surface roughness and friction. As described in chapter 3, we considered factors such as layer height, infill density, and the relative alignment of printed layers. This analysis provided valuable insights into how manufacturing decisions influence the tribological behavior of FDM-printed components.

Our findings revealed that the frictional behavior of FDM-printed surfaces exhibits deviations from the predictions of conventional friction models, such as the Coulomb-Amontons (CA) and Tabor-Bowden (TB) models. These models, developed for relatively smooth and homogeneous surfaces, often can not capture the complex interactions between the textured and anisotropic surfaces of AM parts. For instance, we observed that friction force does not always increase linearly with normal force and can exhibit a non-monotonic relationship with sliding speed (figure 5.1).

In line with objective 9, we evaluated existing friction models and ex-

plored advanced contact mechanics models to develop a modified model that predicts friction behavior in additively manufactured surfaces. As elaborated in chapter 3, this modified model incorporates the effects of surface roughness, contact area, and sliding speed, demonstrating better coherence with empirical data compared to conventional models. This research contributes to a deeper understanding of friction in AM materials, enabling more accurate predictions of actuator performance and facilitating the design of robust and efficient control strategies.

The insights gained from the tribological characterization, as highlighted in section 1.4, contributes to the design, control, and performance of 3D-printed mechatronic systems. By understanding the factors influencing friction and wear in AM components, engineers can make more informed decisions regarding material selection, process parameters, and design modifications to optimize the performance, reliability, and lifespan of these systems. This knowledge is particularly crucial in applications where precision and controllability are paramount, such as surgical robotics and other high-precision mechatronic devices.

The analysis of friction and wear behavior in FDM-printed surfaces, as presented in chapter 3, advances our understanding of tribology in additive manufacturing, provides a foundation for refining friction models, and improving the design and control of 3D-printed actuators for surgical robotics and beyond.

5.4 Modeling and Control

This dissertation addressed research question 4: How can model-based control techniques be optimized to effectively regulate PSM for surgical robots operating within MRI environments, and how do these control strategies enhance surgical precision and safety? The integration of robotics with MRI-guided interventions holds immense promise for enhancing surgical precision and safety. However, achieving precise and reliable motion control within the MRI environment presents significant challenges, particularly when utilizing pneumatic actuators, which exhibit complex nonlinear behavior due to the compressibility of air.

In pursuit of objective 10, a key focus of this research was developing comprehensive models of the pneumatic actuation system, capturing its dynamic behavior, nonlinearities, and interactions with the MRI

environment. As detailed in chapter 4, we employed both theoretical analysis and experimental identification procedures to create models that accurately represented the system's response to various inputs, including pressure signals, external loads, and disturbances. This modeling effort involved considering the dynamics of the pneumatic components, such as valves, cylinders, and tubing, as well as the frictional characteristics of the system, which were informed by our tribological studies presented in chapter 3.

Addressing objective 11, we designed and implemented model-based control strategies to achieve precise and robust position control of the pneumatic actuators. As elaborated in chapter 4, we explored various control techniques, including feedforward control, which uses the model to predict the actuator's response and preemptively compensate for anticipated disturbances, and feedback control, which utilizes sensor data to monitor the system's actual behavior and adjust the control signals accordingly. The choice of control strategy was guided by the specific requirements of the surgical task, the limitations of the MRI environment (e.g., low frame rate at high resolutions), and the availability of MR-compatible sensors.

To fulfill objective 12, we conducted rigorous experiments and simulations to evaluate the performance of the developed control system, assessing its accuracy, stability, responsiveness, and impact on surgical precision and safety. The experimental evaluations, described in chapter 4, involved using a specialized test setup that allowed us to measure the actuator's motion, force output, and response time under various operating conditions. We also performed simulations to explore the system's behavior in different scenarios, including the presence of external disturbances and model uncertainties.

Our research, as highlighted in section 1.4, demonstrated the feasibility and effectiveness of model-based control techniques for regulating pneumatic actuators in MRI-guided surgical robots. The developed control strategies, combining feedforward and feedback control principles, enabled precise and robust tool placement, even in the presence of nonlinearities and disturbances inherent to pneumatic actuation.

The insights gained from this research, particularly those presented in chapter 4, contribute to advancing the field of MR-compatible surgical

robotics. By developing and implementing control strategies that account for the unique challenges of pneumatic actuation in MRI environments, we have paved the way for more precise, safe, and efficient minimally invasive interventions. These advancements hold significant potential for improving surgical outcomes and patient care in MRI-guided procedures.

5.5 Research Limitations and Scope

While this dissertation achieved its objectives, it is important to acknowledge certain research limitations. Regarding the parametric design approach, there was significant focus on clearance as a parameter, with less exploration of other potentially important dimensions. The aspect ratio of the rectangular piston surfaces (width perpendicular to the crankshaft axis versus height parallel to it) could have been further optimized through theoretical analysis to determine ideal proportions. Similarly, cylinder thickness could have been parametrically explored to balance air leakage against tribological behavior and system predictability. The number of cylinders and overall dimensions were additional parameters that could have influenced efficiency and performance but were not exhaustively investigated.

In terms of hybrid manufacturing, while the research demonstrated successful implementation of FDM combined with CNC machining, other AM technologies were only preliminarily explored. We examined Stereolithography (SLA) using Formlabs machines to prototype some cylinders and pistons, but comprehensive testing of these components was not completed within the scope of this research. Post-processing with acetone to improve surface finish was investigated and partially documented in master student theses, but these results were not published in peer-reviewed journals [1, 2]. Attempts at CNC machining of the cylinders presented challenges due to their delicate, small dimensions and assembly with the crankshaft, which would have required further compromise of the assembly printing concept.

Regarding performance characterization, the results presented are not limited to specific prototypes but represent average results across multiple samples. These performance measurements for torque, resolution, and speed generally aligned with the theoretical framework developed in this research. Additional simulation of hydrodynamics using solvers like OpenFOAM or SU2 was attempted but was not sufficiently developed

for publication. The results presented can be considered representative of the technology developed rather than isolated findings from individual prototypes.

Regarding angular accuracy analysis, while several factors affecting accuracy were investigated in this research, a comprehensive quantitative analysis of their individual contributions was not completed. Factors influencing angular accuracy include resolution (with lower resolution inherently limiting accuracy), system predictability (where pneumatic and tribological unpredictability could lead to skipped steps and permanent errors), and backlash (determined by overall system tolerances). While these factors were studied and partially included in the published work, further analysis of their relative impact and interaction would strengthen future designs.

5.6 Future Directions

This dissertation has contributed to the field of MR-compatible surgical robotics through the development and optimization of novel pneumatic stepper actuators, characterization of 3D-printed surface tribology, and implementation of model-based control strategies for precise tool placement within MRI environments. These contributions illuminate several promising avenues for future research that could further enhance the capabilities and clinical applicability of these technologies.

Building upon our work on pneumatic actuators, future research should explore more advanced parametric design methodologies, potentially leveraging tools like the FreeCAD Python Application Programming Interface (API). This approach could enable the creation of highly customizable actuators tailored to specific surgical applications. Extending the concept of assembly printing to encompass entire motorized mechanisms, including complete robotic systems, presents an exciting avenue for creating more integrated and efficient MR-compatible devices. Future work should also focus on developing novel mechanisms for converting continuous linear motion to discretized rotational movement, potentially increasing the efficiency and precision of PSMs.

Future research in parametric design could focus on developing a digital twin of the system to formalize efficiency and performance mathematically. This would enable comprehensive optimization to identify which

parameters most significantly influence performance and efficiency, and how modifying these parameters affects various cost functions. This approach would allow optimization not only for performance and efficiency but also for manufacturing cost, production time, and application versatility while maintaining appropriate levels of accuracy, precision, and resolution. Finding the optimal trade-off between these factors using a formal mathematical framework represents an ideal direction for expanding the parametric design exploration.

The evolution of manufacturing technologies since this research was completed offers numerous opportunities for investigating alternative hybrid approaches. Future work could explore newer FDM technologies with both Acrylonitrile Butadiene Styrene (ABS) and alternative materials like PolyLactic Acid (PLA), as well as other AM methods such as SLA and Selective Laser Sintering (SLS). Further refinement of post-processing techniques, including improved CNC machining strategies and environmentally controlled chambers for solvent treatment with acetone, holds significant potential. The challenge lies in optimizing these chemical post-processing methods to enhance surface finish without significantly compromising dimensional accuracy and precision. Additionally, exploring the strategic integration of Commercially available Off-The-Shelf (COTS) components could further improve performance while reducing manufacturing complexity.

More comprehensive performance testing could be achieved by further developing the sophisticated test setup created during this research. While the existing qualification tooling incorporated Maxon motors for applying external torque and force/torque sensors for measuring system responses, there remains potential for making this setup more mature and automating the testing process. An enhanced system could automatically test different pressures, stepping frequencies, and signal widths while directly controlling external forces through the motor. This automated approach would allow for more extensive characterization of the actuators across their operational envelope.

To better understand and quantify the factors affecting angular accuracy in pneumatic stepper motors (PSMs), future studies should leverage enhanced qualification tooling with high-resolution position encoders. Beyond measuring accuracy, such studies should also evaluate precision and repeatability across various operational conditions. This would

provide a more complete understanding of the system's performance characteristics and reliability, particularly important for surgical applications where consistent, predictable behavior is essential.

The next phase in advancing these technologies toward clinical implementation should explore the integration of sophisticated imaging modalities, including Diffusion Tensor Imaging (DTI) and functional MRI (fMRI), with the developed robotic platforms. This integration holds immense potential for enhancing surgical guidance and decision-making, particularly in needle-based interventions such as biopsy collection, fiducial marker placement, and brachytherapy seed implantation. By providing real-time information about tissue properties and deformation during needle insertion, including critical parameters such as tissue stiffness, vessel locations, and anatomical boundaries, these imaging techniques could significantly improve procedural safety and accuracy. Such capabilities would enable more precise targeting through neural fiber tracts avoidance in DTI-guided biopsies, real-time monitoring of tissue displacement during needle advancement, and the development of adaptive control strategies that can adjust the robot's insertion trajectory based on the evolving intraoperative situation. This direction represents a natural progression from the precise actuation and control methods developed in this work towards more intelligent and responsive surgical systems optimized for image-guided needle interventions.

Translating these research advancements into clinical practice requires a multifaceted approach that builds upon the foundational work presented in this dissertation. The next steps should include rigorous preclinical validation through animal models and cadaver studies, followed by well-designed clinical trials to demonstrate the safety and efficacy of the developed technologies. Collaboration with industry partners, particularly MRI device manufacturers such as Siemens Healthineers, Philips Healthcare, and GE Healthcare, will be essential to navigate the regulatory landscape and bring these innovations to market. These companies have a vested interest in expanding the capabilities of their MRI systems, potentially transforming them from purely diagnostic devices into platforms for image-guided interventions and surgeries. Such collaborations could facilitate the integration of MR-compatible robotic systems directly into existing MRI suites, effectively turning imaging rooms into advanced surgical environments. Furthermore, developing

intuitive user interfaces, comprehensive training programs, and standardized protocols will be crucial for ensuring the seamless integration of these MR-compatible robotic systems into clinical workflows, making them accessible to surgeons and patients worldwide.

By pursuing these interconnected research directions, we can build upon the findings of this dissertation to create more advanced, reliable, and clinically applicable MR-compatible surgical robotic systems. This holistic approach, encompassing actuation technology, materials science, control systems, imaging integration, and clinical translation, promises to significantly enhance the precision, safety, and efficacy of minimally invasive surgical interventions in the years to come.

Acknowledgments

The journey leading to this dissertation has been profound and filled with moments of insight, perseverance, and collaboration. From 2015 to 2020, I was at the University of Twente, where I worked under the guidance of Prof. Sarthak Misra to explore the fascinating topic of electromagnetically stealth pneumatic actuation.

My deepest gratitude goes to my advisor, Prof. Misra, whose unwavering support, boundless knowledge, and invaluable guidance were cornerstones of my doctoral voyage. His mentorship inspired me through the peaks and valleys of my academic expedition, and I could not have asked for a more exceptional mentor. I vividly remember our brainstorming sessions, where his ability to connect seemingly disparate ideas sparked new research directions and ignited my passion for tackling complex challenges.

I am equally indebted to my dissertation committee members, Prof. Ali Sadeghi, Prof. John J. van den Dobbelsteen, Prof. Ian Gibson, Prof. Matthijn de Rooij, and Prof. Cyril Moers for their time, insightful comments, and feedback that refined my thinking and elevated my work. Their collective

expertise significantly shaped this research outcome.

My academic journey has been enriched by collaborations with exceptional individuals. I extend my sincere thanks to Prof. Mostafa Rostami and Dr. Siamak Farkoush from AmirKabir University of Technology (formerly Tehran Polytechnic) (AUT) in Tehran, Prof. René van de Molengraft, Prof. Maarten Steinbuch, and Prof. Pieter Nuij from the Technical University of Eindhoven (TU/e), and Prof. Jan Broenink, Prof. Jurgen Futterer, Prof. Gijs Krijnen, Prof. Dannis Brouwer, and Prof. Theo de Vries from the Robotics and Mechatronics (RaM) at University of Twente (UT), for their support and collaborative spirit.

I am particularly grateful to the researchers I worked with, including Soheila Roohi and Morteza Mojarradi, whose dedication and contributions were instrumental in advancing various research projects. Their insights and expertise were invaluable in navigating the complexities of our research.

I want to express my sincere appreciation to all the students I have supervised and mentored throughout my research. Their enthusiasm, dedication, and fresh perspectives have enriched my experience and contributed significantly to the success of our projects, paving the way for future advancements in the field. A special thank you goes to Xiaolong Zhi, Vincent Groenhuis, Tomas Johannink, Dinah Kleiboer, Charalambos Rossides, Robert van der Wal, Anne Schrader, and Rihards Belinskis.

I am deeply grateful to my former colleague at the Surgical Robotics Lab, Mert Kaya, for his indispensable support and insightful feedback throughout the writing of this dissertation. His expertise and encouragement were instrumental in shaping the final manuscript. His meticulous attention to detail and constructive criticism helped me refine my arguments and present my research clearly and compellingly.

The financial support that made this research possible deserves special acknowledgment. I am deeply grateful for the generous funding from:

- The UT
- Pioneers in Health-Care (PiHC) Vouchers for:
  - The **Pano**ramatic user interface for navigation and documentation of endoscopic guided **Surg**eries (PanoSurg) project
  - The **Pneu**matically **A**ctuated **R**obot for **M**inimally invasive

MRI-guided interventions (PneuARMM) project

The combined support from these organizations has enabled me to pursue this research and contribute to the advancement of Magnetic Resonance (MR)-compatible surgical robotics.

On a personal note, my heartfelt gratitude goes to my family – my wife, Fariba Ghasemy, and daughter, Liana – for their unwavering love, boundless support, and constant belief in me. They have been my anchor and inspiration, particularly during the most challenging moments of this journey. Their love and encouragement have been the driving force behind my perseverance and dedication.

As I stand at this academic milestone, I am grateful for the experiences, collaborations, and support shaping my doctoral journey. The knowledge and insights gained through this research have strengthened my commitment to innovation and reinforced my dedication to developing technologies that enhance healthcare outcomes. I am eager to apply these experiences and expertise to future challenges, continuing to advance the field of medical robotics and contribute to scientific progress that benefits patient care.

About the Author

Foad Sojoodi Farimani is a driven and accomplished researcher and engineer passionate about pushing the boundaries of medical robotics and mechatronics. His doctoral research at the University of Twente (UT) focused on developing innovative Magnetic Resonance (MR)-compatible pneumatic actuators for surgical applications, addressing a critical challenge in minimally invasive surgery.

Foad's academic journey began at Sharif University of Technology (formerly Aryamehr) (SUT), where he earned a Bachelor of Science in Mechanical Engineering

in 2006. He further honed his skills and knowledge at AmirKabir University of Technology (formerly Tehran Polytechnic) (AUT), obtaining a Master of Science in Biomedical Engineering in 2009. His early research experiences sparked a deep interest in medical robotics, leading him to pursue a Ph.D. at the UT's Surgical Robotics Laboratory (SRL).

During his doctoral studies, Foad exhibited outstanding leadership and technical acumen, leading the charge on multiple pioneering research projects. His work on the McRobot project, a cable-driven robotic system for Magnetic Resonance Imaging (MRI)-guided interventions, showcased his innovative design approach and ability to overcome technical challenges in creating MR-compatible robotic platforms. He further expanded his research horizons at the Technical University of Eindhoven, where he supervised master's students in developing advanced mechanism designs and sensing systems for the McRobot platform.

Continuing his research trajectory at the UT, Foad led diverse research projects. These projects included exploring innovative user interfaces for robotic-assisted surgery, including developing immersive head-mounted displays and augmented reality systems for enhanced surgical visualization and control. One notable project in this area was the **Pano**ramatic user interface for navigation and documentation of endoscopic guided **Surg**eries (PanoSurg) project, a collaboration with Dr. Erik Cornel at Ziekenhuis Groep Twente (ZGT) Hengelo.

Foad's doctoral research culminated in developing the **Pneu**matically **A**ctuated **R**obot for **M**inimally invasive **M**RI-guided interventions (PneuARMM) system, a novel pneumatically actuated robotic system for precise lung interventions under MRI guidance.

Foad's contributions to the field of medical robotics extend beyond academic research. He is the founder and CEO of PneuRobotics, a spin-off company from the UT specializing in developing and commercializing MR-compatible pneumatic actuators. His entrepreneurial spirit and commitment to innovation continue to drive advancements in surgical robotics, making these technologies more accessible and affordable for healthcare providers and patients worldwide. Various awards and grants have recognized Foad's research, including Pioneers in Health-Care (PiHC) vouchers for the PanoSurg and PneuARMM projects.

While Foad's passion for medical robotics remains strong, his career path

turned toward the semiconductor industry in 2020. He joined the supply chain of Advanced Semiconductor Materials Lithography (ASML), a leading provider of lithography systems for the semiconductor industry. He worked at companies such as VDL (van der Leegte) Enabling Technologies Group (ETG) Technology and Development (T&D) as a lead mechanical engineer and then transitioned to NTS (Nebato Te Strake) Development and Engineering (D&E) as a system lead engineer in 2022, applying his expertise in mechatronics, control systems, and precision engineering to advance the manufacturing technologies that underpin the production of microchips.